

Bifurcation Analysis of the Macroscopic Traffic Flow Model Based on Driver's Anticipation and Traffic Jerk Effect

W. H. Ai^{a,*}, L. Xu^a, T. Zhang^a, and D. W. Liu^b

^a College of Computer Science and Engineering, Northwest Normal University, Lanzhou, Gansu, China

^b College of Electrical Engineering, Lanzhou Institute of Technology, Lanzhou, Gansu, China

*e-mail: wenhuan618@163.com

Received June 5, 2023; revised September 7, 2023; accepted October 31, 2023

Abstract—Based on realistic traffic conditions, the macroscopic traffic flow model that considers the driver's anticipation and traffic jerk effect is improved, and the bifurcation theory is used to describe and predict nonlinear traffic phenomena on the road from the perspective of global stability. Firstly, the linear stability conditions and the Korteweg–de Vries–Burgers equation are derived using linear and nonlinear methods to characterize the evolution of traffic flow. The type and stability of the equilibrium solution are discussed using the bifurcation analysis method, and the conditions of existence of the Hopf bifurcation and saddle-node bifurcation are proved. Numerical simulations show that the model can describe the complex nonlinear dynamic phenomena observed on the road. The bifurcation analysis will be helpful for improving our understanding of stop-and-go and sudden changes in stability in real traffic flow.

Keywords: traffic flow, driver's anticipation, traffic jerk, nonlinear analysis, bifurcation analysis

DOI: 10.1134/S0015462823601249

Nowadays, traffic congestion became one serious social problem, which has attracted researchers to develop various models to study it. These include microscopic traffic flow models represented by cellular automata models and car-following models [1–3], as well as macroscopic traffic flow model represented by the continuous models [4, 5].

In 1995, in [6] the optimal velocity model was proposed. This model can be used to explain the qualitative characteristics of the actual traffic flow, such as the stop-and-go phenomenon, the traffic instability and congestion evolution, and so on. Based on the optimal velocity model, many new car-following models have been improved and proposed [7–9].

A macroscopic traffic flow model was first proposed by Lighthill and Whitham [10] in 1955, followed by a similar model by Richards [11], and these two models have been known as the Lighthill, Whitham, and Richards model. This is the forerunner of the macroscopic model, which is simple but has the basic properties of nonlinear traffic flow. Subsequently, in [12, 13] the Payne–Whitham model was constructed. In [14], it was proposed to replace the null derivative of the “pressure” with the convective derivative in the acceleration equation, and later, in [15], the model was improved by introducing a relaxation term to obtain the improved Aw–Rascle model. In [16], a new model with introduction of the velocity field and the shop distance function was proposed, and in [17] a speed gradient model for anisotropic traffic flow was proposed. Subsequent researchers have made various improvements to the base model and obtained various macroscopic models that fit various traffic situations.

Different from the traditional fluid force model, in [18, 19] two models, namely, the instantaneous single-lane traffic flow model and the two-lane unsteady traffic flow model controlled by traffic signals, were proposed. Both models consider self-organization and can describe, both qualitatively and quantitatively, the conditions required for the maximum capacity, and make it possible to analyze the occurrence and evolution of “moving traffic jams” on the road, as well as the impact of road traffic control units.

In recent years, the study of traffic flow evolution on circular roads has become a hot topic. Previous hydrodynamic models could not represent the unidirectional propagation of weak perturbations, nor the constraints on the velocity and acceleration. In [20], the properties of compressible media were introduced to solve the above problem, and a model of irregular single-lane traffic flow model on a circular road was proposed. This model can correctly (qualitatively and quantitatively) describe “the conditions

that ensure the maximum traffic capacity” and “the occurrence and evolution of road traffic jams.” Analogous to non-Newtonian fluids, viscoelastic traffic flow modeling has been used to develop macroscopic continuum models. In [21, 22] the viscoelastic effect in the loop traffic flow model was considered and the sensitivity of traffic flow to viscoelasticity was discussed. This illustrated the potential of viscoelastic traffic flow in predicting actual traffic flow. Over the years (see, e.g., [23, 24]), viscoelastic loop traffic flow models have been continued to explore for successively predicting travel times for loops and factoring traffic stress (emergency and moderate) into loop travel times. Thereafter, in [25] complex factors such as ramps, tunnels, as well as uphill and downhill slopes were considered and a composite ring road model was developed to study the evolution of its traffic flow congestion wave. In [26], a new macroscopic traffic flow model for multi-lane loops was proposed and the impact of freeway operating areas on traffic flow was analyzed.

Many researchers [27–29] have built simulation platforms based on the models in order to study the effects of specific conditions on traffic flow, calculated numerical fluxes using the 5th-order weighted essentially non-oscillatory scheme for spatial discretization, and processed the time derivative term using the 3rd-order Runge–Kutta scheme for the time derivative term.

In many situations, sudden braking and acceleration can lead to a large waste of energy, as well as damage to the car itself, increase exhaust emissions to pollute the environment, and even cause traffic accidents. The temporal dynamics of the acceleration and deceleration of a vehicle are represented by the jerk profile, where jerk [30] is the derivative of the acceleration with respect to time. In this direction, in [31] the jerk in the lattice model was introduced and it was confirmed that the jerk parameter plays an important role in stabilizing the traffic jam efficiently in sensing the flux difference of leading sites. In addition, in [32] a new model for following the chase by considering non-motorized vehicles on the traffic jerk was proposed and it was found that this effect can increase traffic congestion. In a real-world driving environment, drivers often observe the surrounding traffic and adjust their speed according to their expectations. For example, in [33] the traffic anticipation into the car-following model was introduced and a new car-following model for traffic anticipation was proposed and the stability of traffic flow was studied. In [34], the anticipation effects into the two-lane lattice model were introduced and the new model to effectively suppress traffic congestion was obtained.

Up to now, there have been few studies on incorporating the driver’s jerk and anticipation into the continuum model. The traffic jerk and driver anticipation will have a significant impact on the traffic movement. Therefore, this paper establishes a new macro traffic flow model considering both driver’s anticipation and the traffic jerk.

The Burgers equation, as a classical nonlinear development equation, originated from the turbulence theory, which describes a viscous nonlinear transport problem and is used to study the phenomena of surge waves and eddies, etc. In the field of traffic, the Burgers equation is used to describe the propagation behavior of density waves. Before the formation of traffic congestion, nonlinear instability phenomenon will inevitably appear, and various “traffic isolated waves” will appear. In [35], an improved lattice model of traffic flow was proposed and the Burgers equation were derived to describe the density wave in the steady zone, proving that the density difference has an important role in the lattice model. In [36], the Burgers equation was derived for a new hydrodynamic model to describe the propagation behavior of the traffic flow density wave in the stable zone. In [37], the triangular shock wave in the stable zone determined by the Burgers equation by the simplified uptake method was discussed, and it was proved that the model has a positive role in reduction of local clusters.

In contrast to the Burgers equation, the Korteweg–de Vries–Burgers equation, which incorporates the convective and viscous effects of the Burgers equation, as well as the nonlinear dispersion term, permits to study more complex fluctuation phenomena, such as isolated waves and the stability of fluctuating solutions, etc. In 1895, Dutch mathematicians Korteweg and De Vries have studied the motion of small- and medium-amplitude long waves in shallow water, and jointly discovered a partial differential equation of one-way motion of diving waves, called the Korteweg–de Vries equation. The Korteweg–de Vries–Burgers equation has been proposed in the study of liquid flow with bubbles and liquid flow in elastic pipes [38]. In [39], a modified velocity gradient model was proposed and the Korteweg–de Vries–Burgers equation was derived to describe traffic flow near the neutral stability line, which proved that the new model is able to simulate complex traffic phenomena, such as local clustering effects and so on. In [40], an improved traffic flow model was used to derive the Korteweg–de Vries–Burgers equation near the neutral stable line, indicating that the new model can detect the local clustering phenomenon under certain conditions. In [41], the neutral stability condition in the improved macroscopic traffic flow model was obtained and the Korteweg–de Vries–Burgers equation, that proves the rationality of the new model, was derived.

Most of the traffic flow models represent nonlinear equations with parameters, and the study of these models reveals that when the parameters in the models change and cross a certain critical value, the qualitative nature of the traffic system also changes in nature. This is highly consistent with the sudden changes among various traffic phenomena in real traffic, such as the free-flowing state, the vehicle stop-and-go state, the steep traffic capacity reduction, the cluster effect, etc. This transformation between different traffic flow states represents essentially the bifurcation behavior of traffic flow caused by various reasons [42].

Bifurcation is a common class of nonlinear phenomena. For nonlinear dynamical systems, the bifurcation is a phenomenon in which the topology of the system's motion trajectory changes in nature when the system's parameters change and cross a critical value. The research on the bifurcation behavior in traffic flow can well explain various nonlinear phenomena in real traffic, and provide an effective theoretical basis for guiding and developing the planning and control management of traffic systems, to fundamentally alleviate and prevent traffic congestion. In [43], the existence of subcritical Hopf bifurcations was established by showing the coexistence of stable and unstable solutions in the optimal velocity model. In [44], a discrete form of the Payne model was derived and the phenomenon of period-doubling bifurcation and the transformation of traffic flow states in the model was investigated. In [45], the existence of the generalized Hopf or Bautin bifurcations in the Kerner–Konhäuser model was illustrated. In [46] the conditions of existence of the Hopf bifurcation of the velocity gradient macroscopic model were derived, the Hopf bifurcation types and their stability were studied, and the bifurcation theory was used to innovatively explain the nonlinear traffic phenomena in complex ground transportation systems. In [47], the bifurcation analysis was taken into account in railroad models to explore the impact of Hopf bifurcation limit cycles on improving railroad models. In [48], the bifurcation theory was used to analyze a heterogeneous traffic flow model considering transverse time headway. In [49], the existence of bifurcation in the improved model was proved and the traffic phenomena caused by it were analyzed. However, there are a few studies based on macroscopic traffic flow models to analyze traffic flow bifurcation phenomena, and some literature only partially covers this aspect. The bifurcation analysis method has not been widely used in traffic flow theory. Based on the background of the current realistic needs of highway traffic prevention and control, there are problems such as frequent changes in the traffic operation state, the difficulty in determining the mutation point, and the inability to control the mutation point effectively. Therefore, it is of great theoretical value and practical significance to carry out stability modeling of road traffic system and analyze the bifurcation behavior by using the bifurcation theory in nonlinear dynamics.

In the present paper, a macroscopic hydrodynamic model based on the optimal speed model was proposed considering the effects of driver's anticipation and traffic jerk. Linear and bifurcation analyses were performed for this new model using linear and nonlinear theories. Neutral stability conditions were derived using the linear analysis, and the Korteweg–de Vries–Burgers equation was derived to describe variation in the traffic flow congestion density waves near the neutral stability line. In addition, the bifurcation theory within framework of nonlinear dynamics was applied to analyze the congestion and sudden change in stability of the road traffic system caused by bifurcation.

1. MACRO TRAFFIC FLOW MODEL

Each vehicle has an optimal speed, which is determined by the distance between the vehicle itself and the vehicle in front. Based on this concept, in [6] a very classic microscopic traffic flow model, called the optimal velocity model, was proposed. The expression of the model can be written as follows:

$$\frac{dv_n(t)}{dt} = a[V(\Delta x_n(t)) - v_n(t)], \quad (1.1)$$

where a is the sensitivity of a driver, $v_n(t)$ is the instantaneous speed of the vehicle n at time t , $\Delta x_n(t) = x_{n+1}(t) - x_n(t)$ is the headway time distance between vehicle n and vehicle $n + 1$ at the instant t , and $V(\Delta x_n(t))$ is the optimal velocity function defined as follows:

$$V(\Delta x_n(t)) = \frac{V_{\max}}{2\{\tanh[\Delta x_n(t) - h_c] + \tanh(h_c)\}}, \quad (1.2)$$

where V_{\max} and h_c are the maximum speed of the vehicle and the allowed safety distance, respectively.

The driver's anticipation τ and the traffic jerk term are incorporated into the optimal velocity model, at which point a new dynamics equation is obtained as follows:

$$\begin{cases} \frac{dv_n(t)}{dt} = a[V(\Delta x_n(t + \tau) - V_n(t))] - \lambda J_n(t) \\ J_n(t) = \frac{dv_n(t)}{dt} - \frac{dv_n(t-1)}{dt}, \end{cases} \quad (1.3)$$

where $\Delta v_n = v_{n+1} - v_n$ is the speed difference between the front car $n + 1$ and the rear car n , $J_n(t)$ is the jerk factor, represents the jerk effect term for the n th vehicle in traffic at time t . Here, λ represents the jerk parameter, and τ represents the anticipation time. Equation (1.3) shows that the acceleration of the n th vehicle at time t is determined not only by the velocity $V_n(t)$, but also by the anticipation time and the traffic jerk.

Before deriving the continuous medium model, we perform the Taylor expansion on the microscopic variables $\Delta x_n(t + \tau)$ and ignore the higher-order terms, i.e.

$$\Delta x_n(t + \tau) = \Delta x_n(t) + \tau \frac{d\Delta x_n(t)}{dt} = \Delta x_n(t) + \tau \Delta V_n(t), \quad (1.4)$$

thus, $V(\Delta x_n(t + \tau))$ can be written as the following relation:

$$V(\Delta x_n(t + \tau)) = V(\Delta x_n(t)) + \tau \Delta V_n(t) V'(\Delta x_n(t)). \quad (1.5)$$

To facilitate the derivation, we first rewrite Eq. (1.3), i.e., write it in the form:

$$\frac{dv_n(t)}{dt} = a[V(\Delta x_n(t) - V_n(t))] + a\tau \Delta V_n(t) V'(\Delta x_n(t)) - \lambda \left(\frac{dv_n(t)}{dt} - \frac{dv_n(t-1)}{dt} \right). \quad (1.6)$$

To transform the above micro traffic flow model into a macro traffic flow model, the following variables are introduced [50]:

$$\begin{aligned} v_n(t) &\rightarrow v(x, t), & v_{n+1}(t) &\rightarrow v(x + \Delta, t) \\ V(\Delta x_n(t)) &\rightarrow V_e(\rho), & V'(\Delta x_n(t)) &\rightarrow V'(h), & J_n(t) &\rightarrow v(x, t) v_{xt}(x, t), \end{aligned}$$

where Δ represents the distance between two adjacent vehicles, $\rho(x, t)$ and $v(x, t)$ means the macroscopic density and the velocity at position (x, t) . By the density ρ and the average head time distance $h = 1/\rho$, we define the equilibrium velocity $V_e(\rho)$ as well as have $V'(h) = -\rho^2 V_e'(\rho)$. Substituting the above macro variables into Eq. (1.6), we can derive the following equation:

$$\frac{dv(x, t)}{dt} = a[V_e(\rho(x, t) - v(x, t))] - a\tau \rho^2 \Delta V_e'(\rho)[v(x + \Delta, t) - v(x, t)] - \lambda[v(x, t) v_{xt}(x, t)]. \quad (1.7)$$

Expanding Eq. (1.7) and neglecting the nonlinear terms, an approximation of Eq. (1.7) can be obtained as follows:

$$\frac{dv}{dt} = a[V_e(\rho) - v] - a\tau \rho^2 \Delta V_e'(\rho) \left[\frac{\partial v}{\partial x} + \frac{\partial^2 v}{\partial x^2} \right] - \lambda v v_{xt}. \quad (1.8)$$

The above equation is reorganized as:

$$\frac{\partial v}{\partial t} + [v + a\tau \rho^2 \Delta V_e'(\rho)] \frac{\partial v}{\partial x} = a[V_e(\rho) - v] - \lambda v v_{xt} - a\tau \rho^2 \Delta V_e'(\rho) \frac{\partial^2 v}{\partial x^2}. \quad (1.9)$$

The second term on the right-hand side of Eq. (1.9) is a simplification of the jerk factor, and the mixed partial derivative can be thought of as $\partial a/\partial x$ (where a denotes the acceleration), which responds to the physical meaning of the jerk factor.

Combining the conservation equations, we obtain the new macroscopic continuous traffic flow model:

$$\begin{cases} \frac{\partial \rho}{\partial t} + \frac{\partial(\rho v)}{\partial x} = 0 \\ \frac{\partial v}{\partial t} + [v + a\tau \rho^2 \Delta V_e'(\rho)] \frac{\partial v}{\partial x} = a[V_e(\rho) - v] - \lambda v v_{xt} - a\tau \rho^2 \Delta V_e'(\rho) \frac{\partial^2 v}{\partial x^2}. \end{cases} \quad (1.10)$$

2. LINEAR STABILITY ANALYSIS

First, a linear stability analysis is used to study the stability conditions of the shock wave. To facilitate the analysis, we express Eq. (1.10) in the vector form:

$$\frac{\partial \mathbf{U}}{\partial t} + \mathbf{A} \frac{\partial \mathbf{U}}{\partial x} = \mathbf{E}, \tag{2.1}$$

where

$$\mathbf{U} = \begin{bmatrix} \rho \\ v \end{bmatrix}, \quad \mathbf{A} = \begin{bmatrix} v & \rho \\ 0 & v + a\tau\rho^2\Delta V_e'(\rho) \end{bmatrix}, \tag{2.2}$$

$$\mathbf{E} = \begin{bmatrix} 0 \\ a[V_e(\rho) - v] - \lambda v v_{,xt} - a\tau\rho^2\Delta V_e'(\rho) \frac{\partial^2 v}{\partial x^2} \end{bmatrix}. \tag{2.3}$$

The eigenvalues of \mathbf{A} can be easily obtained by finding the roots of the following equation:

$$|\lambda \mathbf{I} - \mathbf{A}| = 0, \tag{2.4}$$

where \mathbf{I} represents the unit matrix. Then the characteristic velocity is obtained as follows:

$$\lambda_1 = v, \quad \lambda_2 = v + a\tau\rho^2\Delta V_e'(\rho). \tag{2.5}$$

It is easy to conclude that the characteristic velocity λ_i ($i = 1, 2$) is lower than the macroscopic traffic flow velocity v . The speed of traffic flow in a high-density roadway will be lower than that in a low-density roadway. Since the equilibrium velocity $V_e(\rho)$ is a monotonically decreasing function for the density, i.e., $V_e'(\rho) < 0$, this indicates that the model has the anisotropic property of the traffic flow.

Then the qualitative properties of the model are analyzed using the linear stability analysis. Considering that the traffic flow steady state is homogeneous, small perturbations are applied to the homogeneous flow [51, 52]:

$$\begin{pmatrix} \rho(x, t) \\ v(x, t) \end{pmatrix} = \begin{pmatrix} \rho_0 \\ v_0 \end{pmatrix} + \begin{pmatrix} \hat{\rho}_k \\ \hat{v}_k \end{pmatrix} \exp(ikx + \sigma_k t). \tag{2.6}$$

Substituting equation (2.6) into equation (1.10) and neglecting the nonlinear term for small perturbations, we obtain:

$$(\sigma_k + v_0 ik) \hat{\rho}_k + \rho_0 ik \hat{v}_k = 0, \tag{2.7}$$

$$\sigma_k \hat{v}_k + \hat{v}_k (v_0 + a\tau\rho_0^2\Delta V_e'(\rho_0)) ik = a[V_e'(\rho_0) \hat{\rho}_k - \hat{v}_k] - \lambda v_0 \hat{v}_k ik \sigma_k - (ik)^2 a\tau\rho_0^2\Delta V_e'(\rho_0). \tag{2.8}$$

The following equation can be obtained after some algebra:

$$\begin{cases} (\sigma_k + v_0 ik) \hat{\rho}_k + \rho_0 ik \hat{v}_k = 0 \\ aV_e'(\rho_0) - [\sigma_k + a + (v_0 + a\tau\rho_0^2\Delta V_e'(\rho_0) + \lambda v_0 \sigma_k) ik - (ik)^2 a\tau\rho_0^2\Delta V_e'(\rho_0)] \hat{v}_k = 0. \end{cases} \tag{2.9}$$

If there exists a non-zero solution to Eq. (2.9), then the determinant of its coefficient matrix must be equal to zero:

$$\begin{vmatrix} \sigma_k + v_0 ik & \rho_0 ik \\ aV_e'(\rho_0) - [(\sigma_k + v_0 ik) + (a\tau\rho_0^2\Delta V_e'(\rho_0) + \lambda v_0 \sigma_k) ik + a - (ik)^2 a\tau\rho_0^2\Delta V_e'(\rho_0)] & \end{vmatrix} = 0, \tag{2.10}$$

so, we can obtain that σ_k must satisfy the following quadratic equation:

$$(\sigma_k + v_0 ik)^2 + aV_e'(\rho_0) \rho_0 ik + (\sigma_k + v_0 ik)[a + ik(\lambda v_0 \sigma_k + a\tau\rho_0^2\Delta V_e'(\rho_0)(ik - 1))] = 0. \tag{2.11}$$

We will consider the long-wave expansion, i.e., $ik \approx 0$. Let $\sigma_k = \sigma_1 ik + \sigma_2 (ik)^2 + \dots$, and we will substitute this relation in Eq. (2.11); then we can get the second-order expression for ik :

$$[aV_e'(\rho_0) \rho_0 + (\sigma_1 + v_0) a] ik + [(\sigma_1 + v_0)^2 + \sigma_2 a + \lambda v_0 \sigma_1 - (\sigma_1 + v_0) a\tau\rho_0^2\Delta V_e'(\rho_0)] (ik)^2 = 0. \tag{2.12}$$

To ensure that Eq. (2.12) above holds, the first-order term ik and the second-order term $(ik)^2$ of the power series must be equal to zero:

$$aV_e'(\rho_0)\rho_0 + (\sigma_1 + v_0)a = 0, \quad (2.13)$$

$$(\sigma_1 + v_0)^2 + \sigma_2 a - (\sigma_1 + v_0)a\tau\rho_0^2\Delta V_e'(\rho_0) = 0. \quad (2.14)$$

According to Eqs. (2.13) and (2.14) above, the coefficients of ik and $(ik)^2$ can be obtained as follows:

$$\sigma_1 = -v_0 - V_e'(\rho_0)\rho_0, \quad (2.15)$$

$$\sigma_2 = -\frac{V_e'(\rho_0)\rho_0}{a}[V_e'(\rho_0)\rho_0 - \lambda v_0 + a\tau\rho_0^2\Delta V_e'(\rho_0)] + \frac{\lambda v_0^2}{a}. \quad (2.16)$$

When $\sigma_2 > 0$, the traffic flow is stable, and the neutral stability condition is as follows:

$$a_s = \frac{V_e'(\rho_0)\rho_0 - \lambda v_0}{a\tau\rho_0^2\Delta V_e'(\rho_0)}, \quad (2.17)$$

$$\text{Im}(\sigma_k) = -k[v_0 + \rho_0 V_e'(\rho_0)] + O(k^3). \quad (2.18)$$

From Eq. (2.18), it can be deduced that the propagation speed of the disturbance is equal to

$$c(\rho_0) = v_0 + \rho_0 V_e'(\rho_0), \quad (2.19)$$

this is consistent with the kinematic wave velocities mentioned in the literature [53].

3. NONLINEAR ANALYSIS

3.1. Korteweg–de Vries–Burgers Equation

In this section, the Korteweg–de Vries–Burgers equation is derived, and isolated wave solutions are found. Based on the characteristics of the new model, we will perform the following derivation.

To study the properties of the model under the neutral stability conditions, a new coordinate system is introduced [54]:

$$z = x - ct. \quad (3.1)$$

Substituting Eq. (3.1) into the new model (1.10), we can obtain:

$$-c\rho_z + q_z = 0, \quad (3.2)$$

$$-cv_z + (v + a\tau\rho^2\Delta V_e')v_z = a[Ve(\rho) - v] - \lambda v(-cv_{zz}) - a\tau\rho^2\Delta V_e'v_{zz}, \quad (3.3)$$

where the traffic flow q is the product of the density and the speed, the relationship among the three parameters is $q = \rho v$. When the relationship is substituted in formula (3.2), we can obtain

$$v_z = \frac{c\rho_z}{\rho} - \frac{q\rho_z}{\rho^2}. \quad (3.4)$$

The second-order Taylor expansion for the traffic flow q can be expressed as follows:

$$q = \rho Ve(\rho_0) + b_1\rho_z + b_2\rho_{zz}. \quad (3.5)$$

The first term on the right-hand side in relation (3.5) above represents a uniform and stable state quantity in the traffic flow. The parameters b_1 and b_2 can be obtained by substituting relation (3.5) in Eq. (3.3) and then by balancing the coefficients of ρ_z and ρ_{zz} . After substitution, the equation takes the form:

$$\begin{aligned} & -c\left(\frac{c\rho_z}{\rho} - \frac{q\rho_z}{\rho^2}\right) + \left(\frac{q}{\rho} + a\tau\rho^2\Delta V_e'\right)\left(\frac{c\rho_z}{\rho} - \frac{q\rho_z}{\rho^2}\right) \\ & = a\left[V_e(\rho) - \frac{q}{\rho}\right] + \left(\lambda c\frac{q}{\rho} - a\tau\rho^2\Delta V_e'\right)\left(\frac{c\rho_{zz}}{\rho} - \frac{2c\rho_z^2}{\rho^2} - \frac{q\rho_{zz}}{\rho^2} + \frac{2q\rho_z^2}{\rho^3}\right). \end{aligned} \quad (3.6)$$

Since neither ρ_z nor ρ_{zz} is zero, the coefficients of ρ_z and ρ_{zz} in Eq. (3.6) must be equal to zero, so that the parameters b_1 and b_2 can be obtained as follows:

$$\begin{cases} b_1 = \frac{1}{a}[(c - V_e(\rho))(c - V_e(\rho) - a\tau\rho^2\Delta V_e')] \\ b_2 = \frac{1}{a}[(\lambda c - a\tau\rho^2\Delta V_e')(c - V_e(\rho))]. \end{cases} \tag{3.7}$$

Taking $\rho = \rho_h + \hat{\rho}(x, t)$ near the neutral stability condition, and performing the second-order Taylor expansion in terms of ρ , we obtain

$$\rho V_e(\rho) \approx \rho_h V_e(\rho_h) + (\rho V_e)_\rho|_{\rho=\rho_h} \hat{\rho} + \frac{1}{2}(\rho V_e)_{\rho\rho}|_{\rho=\rho_h} \hat{\rho}^2, \tag{3.8}$$

then, combining Eqs. (3.8) and (3.3) and transforming $\hat{\rho}$ into ρ , we finally obtain

$$-c\rho_z + [(\rho V_e(\rho))_\rho + (\rho V_e(\rho))_{\rho\rho}\rho]\rho_z + b_1\rho_{zz} + b_2\rho_{zzz} = 0. \tag{3.9}$$

To convert Eq. (3.9) into the standard Korteweg–de Vries–Burgers equation, the following transformations need to be introduced:

$$U = -[(\rho V_e)_\rho + (\rho V_e)_{\rho\rho}\rho], \quad X = mx, \quad T = -mt. \tag{3.10}$$

Next, substituting Eq. (3.10) in Eq. (3.9), we obtain the standard Korteweg–de Vries–Burgers equation shown below:

$$U_T + UU_X - mb_1U_{XX} - m^2b_2U_{XXX} = 0. \tag{3.11}$$

An analytical solution of the above Korteweg–de Vries–Burgers equation is as follows:

$$U = -\frac{3(-mb_1)^2}{25(-m^2b_2)} \left[\begin{aligned} &1 + 2 \tanh\left(\pm \frac{-mb_1}{10m^2}\right) \left(X + \frac{6(-mb_1)^2}{25(-m^2b_2)} T + \zeta_0 \right) \\ &+ \tanh^2\left(\pm \frac{-mb_1}{10m^2}\right) \left(X + \frac{6(-mb_1)^2}{25(-m^2b_2)} T + \zeta_0 \right) \end{aligned} \right], \tag{3.12}$$

where ζ_0 is an arbitrary constant.

3.2. Types of Equilibrium Points and Their Stability

Essentially, instability is a physical prerequisite for bifurcation to occur. Therefore, before the bifurcation analysis, we can study and analyze the equilibrium solution of the improved continuous medium model. In this section, the equilibrium point is investigated through the substitution of traveling wave in the system, and the phase plane near the equilibrium point is plotted. The equilibrium points are compared to be able to better reflect the changes in the stability near different equilibrium points.

Assume that the model has solutions $\rho(z)$ and $v(z)$ in the form of a traveling wave, where $z = x - ct$ and the traveling wave velocity $c < 0$. Substituting them in Eq. (1.10), we can derive the following equations:

$$-c\rho_z + q_z = 0, \tag{3.13}$$

$$-cv_z + (v + a\tau\rho^2\Delta V_e'(\rho))v_z = a[V_e(\rho) - v] - \lambda v(-cv_{zz}) - a\tau\rho^2\Delta V_e'(\rho)v_{zz}. \tag{3.14}$$

The following expressions can be obtained from Eq. (3.13):

$$v_z = \frac{c\rho_z}{\rho} - \frac{q\rho_z}{\rho^2}, \tag{3.15}$$

$$v_{zz} = \left(\frac{c}{\rho} - \frac{q}{\rho^2} \right) \rho_{zz}. \tag{3.16}$$

Substituting v_z and v_{zz} in the above Eq. (3.14), we have

$$\begin{aligned} & -\frac{\rho_z}{\rho^3}q^2 + \left[\frac{(2c - a\tau\rho^2\Delta V_e'(\rho))\rho_z}{\rho^2} + \frac{a}{\rho} + \frac{\left(\lambda c\left(\frac{q}{\rho}\right) - a\tau\rho^2\Delta V_e'(\rho)\right)\rho_{zz}}{2\rho^2} \right] q \\ & = aV_e(\rho) + \frac{c^2 - ca\tau\rho^2\Delta V_e'(\rho)}{\rho}\rho_z + \frac{c(\lambda c(q/\rho) - a\tau\rho^2\Delta V_e'(\rho))}{2\rho}\rho_{zz}. \end{aligned} \quad (3.17)$$

Integrating Eq. (3.13) in respect to z , we obtain

$$-c\rho + q = \text{const} = q_*. \quad (3.18)$$

To facilitate the calculation, we carry out the conversion of the equation.

$$q = q_* + c\rho. \quad (3.19)$$

Substituting Eq. (3.19) in Eq. (3.17), the following expression can be obtained:

$$\begin{aligned} & \left[a\tau\rho^2\Delta V_e'(\rho)\rho + \left(-a\tau\rho^2\Delta V_e'(\rho) - \frac{\lambda c}{\rho} \right) (q_* + c\rho) + \frac{\lambda c\rho_{zz}}{\rho^3} (q_* + c\rho)^2 \right] \rho_{zz} \\ & - \left[\frac{(q_* + c\rho)^2}{\rho^3} + \left(\frac{c^2}{\rho} - a\tau\rho^2\Delta V_e'(\rho) \right) - \left(\frac{2c}{\rho^2} - a\tau\rho^2\Delta V_e'(\rho) \right) (q_* + c\rho) \right] + a(q_* + c\rho) - aV_e(\rho) = 0. \end{aligned} \quad (3.20)$$

The second-order ordinary differential equation for $\rho(z)$ can be obtained after some algebra

$$\rho_{zz} - G(\rho, c, q_*)\rho_z - F(\rho, c, q_*) = 0, \quad (3.21)$$

where

$$G(\rho, c, q_*) = \frac{\rho\left(\frac{q_*}{\rho} + a\tau\rho^2\Delta V_e'(\rho)\right)}{\lambda cq_* - a\tau\rho^3\Delta V_e'(\rho)}, \quad (3.22)$$

$$F(\rho, c, q_*) = -\frac{a\rho^2(q_* + c\rho - \rho V_e(\rho))}{[\lambda cq_* - a\tau\rho^3\Delta V_e'(\rho)]q_*}. \quad (3.23)$$

Setting $y = \frac{d\rho}{dz}$, Eq. (3.21) can be transformed into a nonlinear dynamical system in the form of a system of first-order ordinary differential equations as shown below:

$$\begin{cases} \frac{d\rho}{dz} = y \\ \frac{dy}{dz} = G(\rho, c, q_*)y + F(\rho, c, q_*). \end{cases} \quad (3.24)$$

Letting the right end term of the system of equations (3.24) be equal to zero, we can obtain that $y = 0$ and $F = 0$, from which we can determine its equilibrium point $(\rho_i, 0)$. Performing the Taylor expansion of the system of equations (3.24) at the equilibrium point $(\rho_i, 0)$, we can obtain the following linear system:

$$\begin{cases} \rho' = y, \\ y' = G(\rho_i, c, q_*)y + F'(\rho_i, c, q_*)(\rho - \rho_i). \end{cases} \quad (3.25)$$

At the equilibrium point $(\rho_i, 0)$, the Jacobian matrix of the system (3.24) can be obtained as follows:

$$L = \begin{bmatrix} 0 & 1 \\ F'_i & G'_i \end{bmatrix}; \quad (3.26)$$

therefore, the corresponding Jacobian characteristic equation takes the form:

$$\lambda^2 - G'_i\lambda - F'_i = 0. \quad (3.27)$$

Introducing the notation $G_i = G(\rho_i, c, q_*)$ and $F_i' = F'(\rho_i, c, q_*)$, from Eqs. (3.22) and (3.23) we can obtain the following results:

$$F_i' = -\frac{a\rho_i^2(c - \rho_i V_e'(\rho_i) - V_e(\rho_i))}{[\lambda c q_* - a\tau\rho_i^3 \Delta V_e'(\rho_i)]q_*}, \tag{3.28}$$

$$G_i = \frac{\rho_i \left(\frac{q_*}{\rho_i} + a\tau\rho_i^2 \Delta V_e'(\rho_i) \right)}{\lambda c q_* - a\tau\rho_i^3 \Delta V_e'(\rho_i)}. \tag{3.29}$$

Since $F = 0$ at the equilibrium point, it follows that $q_* + c\rho_i - \rho_i V_e'(\rho_i) = 0$, so F_i' can be written as:

$$F_i' = \frac{a(q_* + \rho_i^2 V_e'(\rho_i))\rho_i^2}{[\lambda c q_* - a\tau\rho_i^3 \Delta V_e'(\rho_i)]q_*}. \tag{3.30}$$

The type of the equilibrium point of the system can be determined based on the qualitative theory of differential equations: (a) when $F_i' > 0$, the equilibrium point is the saddle point; (b) when $G_i^2 + 4F_i' > 0$ and $F_i' < 0$, the equilibrium point is the node; (c) when $G_i^2 + 4F_i' < 0$ and $G_i^2 \neq 0$, the equilibrium point is the focal point; (d) when $F_i' < 0$ and $G_i^2 = 0$, the equilibrium point is the core center. As $z \rightarrow \pm\infty$, the linear systems are unstable at the saddle point; when $G_i^2 < 0$ (or $G_i^2 > 0$), the stability at the node or focal point is steady, as $z \rightarrow +\infty$ (or $z \rightarrow -\infty$).

From the Hartman–Grobman linearization theorem [55] it follows that the nonlinear system (3.24) has the same equilibrium points as the linear system (3.25). For the equilibrium point which is not the center, the stability situation at the equilibrium point is the same as that for the nonlinear system (3.24) and the linear system (3.25). The equilibrium point ρ_i ($i = 1, 2, 3$) of the linear system (3.24) can be solved when given any set of values of the traveling wave velocity c and the traveling wave parameter q_* . The equilibrium velocity function proposed in the literature is taken as follows [56]:

$$V_e(\rho) = V_f \left\{ \left[1 + \exp\left(\frac{\rho/\rho_m - 0.25}{0.06}\right) \right]^{-1} - 3.72 \times 10^{-6} \right\}, \tag{3.31}$$

where V_f is the free-stream flow velocity and ρ_m is the maximum or the congestion density.

The values of each parameter in the model are given below:

$$v_f = 30 \text{ m/s}, \quad \rho_m = 0.2 \text{ veh/m}, \quad T = 10 \text{ s}, \quad \tau = 2 \text{ s}, \quad \lambda = 0.3, \quad \text{and} \quad \Delta = 100 \text{ m}.$$

Through the derivation of the model, equations (3.22) and (3.23) are obtained that can be used to solve and determine the type and stability of the equilibrium point of the system. As shown in Table 1, the equilibrium point is represented by the following equation, and we choose two sets of parameters from the table to model the stability of the nonlinear system (3.24) at the equilibrium point ρ_i ($i = 1, 2, 3$).

Figure 1a corresponds to the first case in Table 1. There are three equilibrium points, where $(\rho_1, 0)$ and $(\rho_3, 0)$ are the saddle points, and, as $z \rightarrow \pm\infty$, the trajectory in its vicinity is far from the point, at which time the system is unstable. In this case, $(\rho_2, 0)$ is the spiral point, and several spiral trajectories near the saddle point converge to $(\rho_2, 0)$ as $z \rightarrow +\infty$, indicating that the system is stable at this point as $z \rightarrow +\infty$; as $z \rightarrow -\infty$, these trajectories move away from the spiral point and eventually converge, indicating that the system is unstable at that point again and can be seen as a saddle-point-spiral-point-saddle-point solution of the system. The trajectory in the phase plane shows the distribution of saddle plane curves near the saddle point. The area between the two points is determined by the interaction of the spiral and saddle points, and the trajectory shows a combination of the spiral and saddle curve distributions.

Figure 1b corresponds to the second case in Table 1. As can be seen from this figure, there is only a single equilibrium point. The spiral trajectory from $(0.049, 0)$ tends to $(\rho_1, 0)$, as $z \rightarrow +\infty$, indicating that the system is stable; as $z \rightarrow -\infty$, the trajectory is far from $(\rho_1, 0)$, and the system is unstable. Further study shows that the spiral trajectory starting from $(0.045, 0)$ converges very closely to the periphery of the spiral, as shown in Fig. 1b, and the trajectory trend is consistent as $z \rightarrow +\infty$. The results show that there exists

Table 1. Types of equilibrium points and their stability for a given model parameter, $\Delta_i = G_i^2 + 4F_i'$, $i = 1, 2, 3$

	ρ_1	ρ_2	ρ_3
$(c_0, q_*) = (-1.371, 0.2)$	0.0065 $F_i' > 0$, saddle point, unstable for $z \rightarrow \pm\infty$	0.0938 $\Delta_i < 0, G_i < 0$, spiral point, stable for $z \rightarrow +\infty$, unstable for $z \rightarrow -\infty$	0.1447 $F_i' > 0$, saddle point, unstable for $z \rightarrow \pm\infty$
$(c_0, q_*) = (-1.38, 0.64)$	0.0594 $\Delta_i < 0, G_i < 0$, spiral point, stable for $z \rightarrow +\infty$, unstable for $z \rightarrow -\infty$		

a limit ring at the junction of this spiral with the periphery and the orbit tending to $(\rho_1, 0)$ can be regarded as the limit-ring spiral point solution.

3.3. Stationary Solution for Traffic Flow

When the traffic system reaches a balanced and stable state, the vehicle density and speed on the entire road section do not vary with time. Especially when the traffic system reaches some special equilibrium point, the density and speed values on the whole road section will not vary with change in time and road section, and then two static solutions will appear.

The first is the low density and high-speed traffic flow. In this state, there are a few vehicles, and the traffic is smooth. The acceleration and deceleration of a single vehicle does not affect the running of other vehicles or the overall road condition. The second type is the high-density and low-speed traffic flow. In this state, the car speed is slow, the traffic flow density is large, the workshop distance is small, and the speed of a single vehicle will be consistent with the front car as far as possible during the journey. The overall traffic flow keeps a low speed to form a stable traffic flow. To discuss the stability of these two static solutions, the equation for the equilibrium point of the system is analyzed in this subsection.

First, we carry out the traveling wave substitution for model (1.10). Suppose the model has a traveling wave solution $\rho(z)$ and $v(z)$, where $z = x - ct$ and traveling wave velocity $c < 0$. System (1.10) is replaced by traveling wave to obtain the following formula:

$$\begin{cases} \frac{\partial \rho}{\partial z} \times \frac{\partial z}{\partial t} + \frac{\partial(\rho v)}{\partial x} = 0 \\ \frac{\partial v}{\partial z} \times \frac{\partial z}{\partial t} + [v + a\tau\rho^2\Delta V_e'(\rho)] \frac{\partial v}{\partial z} \times \frac{\partial z}{\partial x} = a[V_e(\rho) - v] - \lambda v \left(-c \frac{\partial^2 v}{\partial z^2}\right) - a\tau\rho^2\Delta V_e'(\rho) \frac{\partial^2 v}{\partial z^2}. \end{cases} \quad (3.32)$$

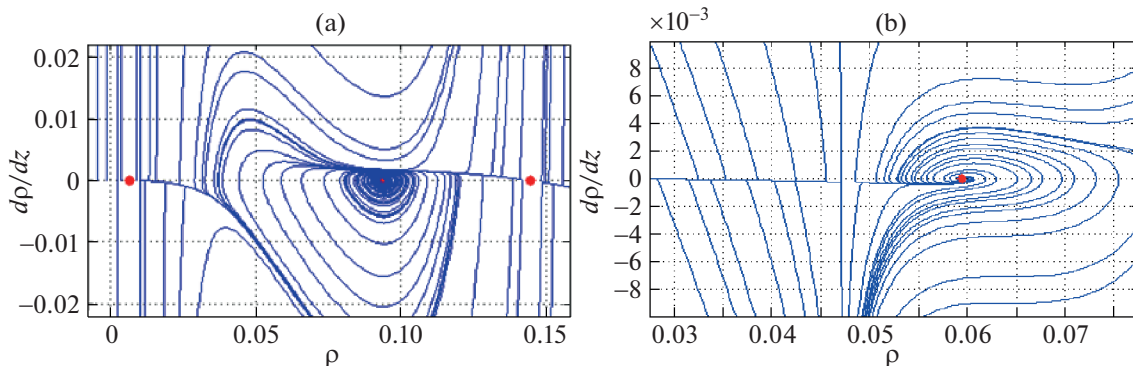


Fig. 1. Trajectories in the ρ - y phase plane with the parameters: (a) $c = -1.371$ and $q_* = 0.2$; (b) $c = -1.38$ and $q_* = 0.64$.

When the system reaches equilibrium and does not change over time, the expression is as follows:

$$\begin{cases} \frac{\partial \rho}{\partial t} = 0, \\ \frac{\partial v}{\partial t} = 0. \end{cases} \tag{3.33}$$

The system of equations (3.33) can be converted to

$$\begin{cases} \frac{\partial \rho}{\partial z} \times \frac{\partial z}{\partial t} = 0, \\ \frac{\partial v}{\partial t} \times \frac{\partial z}{\partial t} = 0. \end{cases} \tag{3.34}$$

Because $z = x - ct$, we have $\frac{\partial \rho}{\partial z} = 0$ and $\frac{\partial v}{\partial t} = 0$. Substituting (1.10) gives the following formula,

$$\begin{cases} \frac{\partial(\rho v)}{\partial x} = 0, \\ a[V_e(\rho) - v] = 0, \end{cases} \tag{3.35}$$

hence we have $V_e(\rho) = v$.

From this we can conclude that when the traffic flow reaches a balanced state, the density and the speed on the entire road section do not change with time or with the change in the road section, the vehicle speed at this time has the density corresponding to the equilibrium speed. Under actual traffic conditions, if the initial density on the road section is a uniform density and the vehicle speed is less than the equilibrium speed, the speed will gradually increase to the equilibrium speed and then remain unchanged. On the contrary, if the initial speed is greater than the equilibrium speed, the vehicle speed will gradually decrease to the equilibrium speed and then remain unchanged. The densities along road segments also do not vary over time.

3.4. Bifurcation Analysis—Proof of the Existence of Hopf Bifurcation Conditions

Lemma 1 [57]: Consider a system of the form $\dot{\mathbf{x}} = f(\mathbf{x}, \lambda)$, $\mathbf{x} \in R^n$, $\lambda \in R$, where λ is a variable parameter. If $f(\mathbf{x}_0, \lambda)$ satisfies the balance condition $f(\mathbf{x}_0, \lambda_0) = \mathbf{0}_{n \times 1}$, let $L = D_x f(\mathbf{x}, \lambda)|_{(\mathbf{x}_0, \lambda_0)}$, and the eigenvalues of the system be $\alpha(\lambda) \pm i\beta$; further, if the system satisfies the following conditions: $\alpha(\lambda_0) = 0$, $\beta(\lambda_0) = \omega > 0$, and $c = \dot{\alpha}(\lambda)|_{\lambda_0} \neq 0$, then the system has a Hopf bifurcation at $\lambda = \lambda_0$.

For the nonlinear dynamical system (3.24), let q_* be a variable parameter that has equilibrium points $(\rho_0, 0)$ for all q_* . At the equilibrium point, the derivative operator matrix L is also the Jacobian matrix of the system at the equilibrium point, as follows:

$$L(q_*) = \begin{pmatrix} 0 & 1 \\ \frac{a(q_* + \rho^2 V_e(\rho))\rho^2}{[\lambda c q_* - a\tau\rho^3 \Delta V_e'(\rho)]q_*} & \frac{(q_* + a\tau\rho^3 \Delta V_e'(\rho))}{\lambda c q_* - a\tau\rho^3 \Delta V_e'(\rho)} \end{pmatrix} \Bigg|_{\substack{\rho=\rho_0 \\ q_*=q_{*0}}} \triangleq \begin{pmatrix} A_1 & A_2 \\ A_3 & A_4 \end{pmatrix}. \tag{3.36}$$

Let its eigenvalue be λ , $\lambda = \alpha(q_*) \pm j\beta(q_*)$, then its characteristic equation is:

$$\lambda^2 - (A_1 + A_4)\lambda + (A_1 A_4 - A_2 A_3) = 0. \tag{3.37}$$

Let the pair of complex eigenvalues of this equation be $\alpha(q_*) \pm j\beta(q_*)$. By solving the characteristic equation, we have:

$$\alpha(q_*) = \frac{A_1 + A_4}{2} = \frac{(q_* + a\tau\rho^3 \Delta V_e'(\rho))}{2(\lambda c q_* - a\tau\rho^3 \Delta V_e'(\rho))}, \tag{3.38}$$

$$\beta(q_*) = \sqrt{(A_1A_4 - A_2A_3) - \frac{(A_1 + A_4)^2}{4}} = \sqrt{\frac{-a(q_* + \rho^2V_e(\rho))\rho^2}{[\lambda cq_* - a\tau\rho^3\Delta V_e'(\rho)]q_*} - \frac{\rho^2\left(\frac{q_*}{\rho} + a\tau\rho^2\Delta V_e'(\rho)\right)^2}{4(\lambda cq_* - a\tau\rho^3\Delta V_e'(\rho))^2}}, \tag{3.39}$$

$$c = \dot{a}(q_*)|_{q_{*0}} = \frac{1}{2(\lambda cq_* - a\tau\rho^3\Delta V_e'(\rho))} \neq 0. \tag{3.40}$$

Let $\alpha(\rho_0, q_{*0}) = 0$,

$$\alpha(\rho_0, q_{*0}) = \left(\frac{(q_* + a\tau\rho_0^3\Delta V_e'(\rho_0))}{2(\lambda cq_* - a\tau\rho_0^3\Delta V_e'(\rho_0))} \right) \Big|_{q_*=q_{*0}} \triangleq 0. \tag{3.41}$$

Thus, we can obtain,

$$q_{*0} = -a\tau\rho^2\Delta V_e'(\rho)\rho_0; \tag{3.42}$$

at the same time,

$$\beta(\rho_0, q_{*0}) = \sqrt{\frac{-a(q_* + \rho^2V_e(\rho))\rho^2}{[\lambda cq_* - a\tau\rho^3\Delta V_e'(\rho)]q_*} - \frac{\rho^2\left(\frac{q_*}{\rho} + a\tau\rho^2\Delta V_e'(\rho)\right)^2}{4(\lambda cq_* - a\tau\rho^3\Delta V_e'(\rho))^2}} \Big|_{\substack{\rho=\rho_0 \\ q_*=q_{*0}}}. \tag{3.43}$$

From Eq. (3.42), we have:

$$\beta(\rho_0, q_{*0}) = \sqrt{\frac{-a(q_* + \rho^2V_e(\rho))\rho^2}{[\lambda cq_* - a\tau\rho^3\Delta V_e'(\rho)]q_*}}. \tag{3.44}$$

Since $V_e'(\rho) < 0$, then we have $\beta(\rho_0, q_{*0}) > 0$, when $-\rho_0^2V_e(\rho_0) > q_{*0} > 0$. At this point, the system has a Hopf bifurcation at $q_* = q_{*0}$.

3.5. Bifurcation Analysis—Proof of the Existence of Saddle-Node Bifurcation Conditions

Lemma 2 [58]: Consider the system $x' = f(x, \lambda)$, $x \in R^n$, $\lambda \in R$, where λ is a variable parameter. If (x_0, λ) satisfies the balance condition $f(x, \lambda)|_{(x_0, \lambda_0)} = 0_{n \times 1}$, set $L = D_x f(x, \lambda)|_{(x_0, \lambda_0)}$. Let α and β be the left and right unit eigenvectors of L , respectively, then $\alpha L = 0$ and $L\beta = 0$. Then $\lambda = \lambda_0$ is a saddle-node type bifurcation of the system when the following conditions are satisfied:

$$i) a = \alpha \cdot \frac{\partial}{\partial \lambda} f(x, \lambda) \Big|_{(x_0, \lambda_0)} \neq 0, \tag{3.45}$$

$$ii) b = \alpha \cdot \sum_{i=1}^n e_i \left[\beta^T \frac{\partial^2}{\partial x^2} f(x, \lambda) \Big|_{(x_0, \lambda_0)} \beta \right] \neq 0. \tag{3.46}$$

For any small $\varepsilon > 0$, the approximate expression for its solution curve near (x_0, λ_0) is as follows:

$$x = \varepsilon\beta + o(\varepsilon^2), \quad \lambda = \frac{\varepsilon^2 b}{2a} + o(\varepsilon^3). \tag{3.47}$$

For the system (3.24), let q_* be a variable parameter and the derivative submatrix at the equilibrium point is shown in Eq. (3.36). When $q_{*0} = -\rho_0^2V_e(\rho_0)$, there is a vector $\beta = \begin{pmatrix} 1 \\ 0 \end{pmatrix}$ that satisfies the equation $L\beta = 0$. Then, we have

$$\alpha \mathbf{L} = 0 \Rightarrow \alpha = \begin{pmatrix} \frac{(q_* + a\tau\rho_0^3\Delta V_e'(\rho_0))}{\lambda cq_* - a\tau\rho_0^3\Delta V_e'(\rho_0)} & 1 \end{pmatrix}. \tag{3.48}$$

Substituting the variables α and β in Eqs. (3.45) and (3.46), we obtain:

$$\begin{aligned} a = \alpha \cdot \frac{\partial}{\partial q_*} \mathbf{f}(\mathbf{x}, q_*) \Big|_{(x_0, q_0)} &= \begin{pmatrix} \frac{(q_* + a\tau\rho_0^3\Delta V_e'(\rho_0))}{\lambda cq_* - a\tau\rho_0^3\Delta V_e'(\rho_0)} & 1 \end{pmatrix} \begin{pmatrix} 0 \\ -\frac{a\rho_0}{[\lambda cq_{*0} - a\tau\rho_0^3\Delta V_e'(\rho_0)]q_{*0}} \end{pmatrix} \\ &= -\frac{a\rho_0}{[\lambda cq_{*0} - a\tau\rho_0^3\Delta V_e'(\rho_0)]q_{*0}} \neq 0, \\ b = \alpha \cdot \sum_{i=1}^n e_i \left[\beta^T \frac{\partial^2}{\partial \mathbf{x}^2} f_i(\mathbf{x}, \lambda) \Big|_{(x_0, \lambda_0)} \beta \right] &= \begin{pmatrix} \frac{(q_* + a\tau\rho_0^3\Delta V_e'(\rho_0))}{\lambda cq_* - a\tau\rho_0^3\Delta V_e'(\rho_0)} & 1 \end{pmatrix} \\ &\times \begin{pmatrix} [1 \ 0] \begin{bmatrix} 0 & 0 \\ 0 & 0 \end{bmatrix} \begin{bmatrix} 1 \\ 0 \end{bmatrix} \\ \frac{a[2V_e(\rho_0) + 4\rho_0 V_e'(\rho_0) + \rho_0^2 V_e''(\rho_0) - 2c]}{[\lambda cq_{*0} - a\tau\rho_0^3\Delta V_e'(\rho_0)]q_{*0}} \frac{-q_{*0}}{[\lambda cq_{*0} - a\tau\rho_0^3\Delta V_e'(\rho_0)]\rho_0^2} \\ -\frac{q_{*0}}{[\lambda cq_{*0} - a\tau\rho_0^3\Delta V_e'(\rho_0)]\rho_0^2} & 0 \end{pmatrix} \begin{bmatrix} 1 \\ 0 \end{bmatrix} \\ &= \frac{a[2V_e(\rho_0) + 4\rho_0 V_e'(\rho_0) + \rho_0^2 V_e''(\rho_0) - 2c]}{[\lambda cq_{*0} - a\tau\rho_0^3\Delta V_e'(\rho_0)]q_{*0}} \neq 0. \end{aligned} \tag{3.49}$$

When $q_{*0} = -\rho_0^2 V_e'(\rho_0)$, the system (3.24) has a saddle-node type bifurcation at $q_* = q_{*0}$.

4. NUMERICAL SIMULATION

4.1. Simulation Considering the Effect of the Initial Density on Traffic Flow

To verify that the newly proposed model can reproduce the stop-and-go phenomenon of real traffic flow at various initial densities, we select traffic flows at various initial densities for simulation experiments. A small local perturbation is added to the homogeneous traffic flow, and then the small perturbation is scaled up so that the stop-and-go phenomenon can be clearly expressed. Considering the case of adding a small local perturbation to the initial uniform traffic flow, the expression for the initial density is given as follows [10]:

$$\rho(x, 0) = \rho_0 + \Delta\rho_0 \left\{ \cosh^{-2} \left[\frac{160}{L} \left(x - \frac{5L}{16} \right) \right] - \frac{1}{4} \cosh^{-2} \left[\frac{40}{L} \left(x - \frac{11L}{32} \right) \right] \right\}, \tag{4.1}$$

$$x \in [0, L],$$

$$v(x, 0) = V(\rho(x, 0)) \quad x \in [0, L], \tag{4.2}$$

where ρ_0 is the initial density, $\Delta\rho_0 = 0.01$ veh/m is the disturbance density, $L = 32.2$ km is the section length, and the dynamic critical condition is given as follows:

$$\rho(1, t) = \rho(2, t), \quad \rho(L, t) = \rho(L - 1, t), \quad v(1, t) = v(2, t), \quad v(L, t) = v(L - 1, t).$$

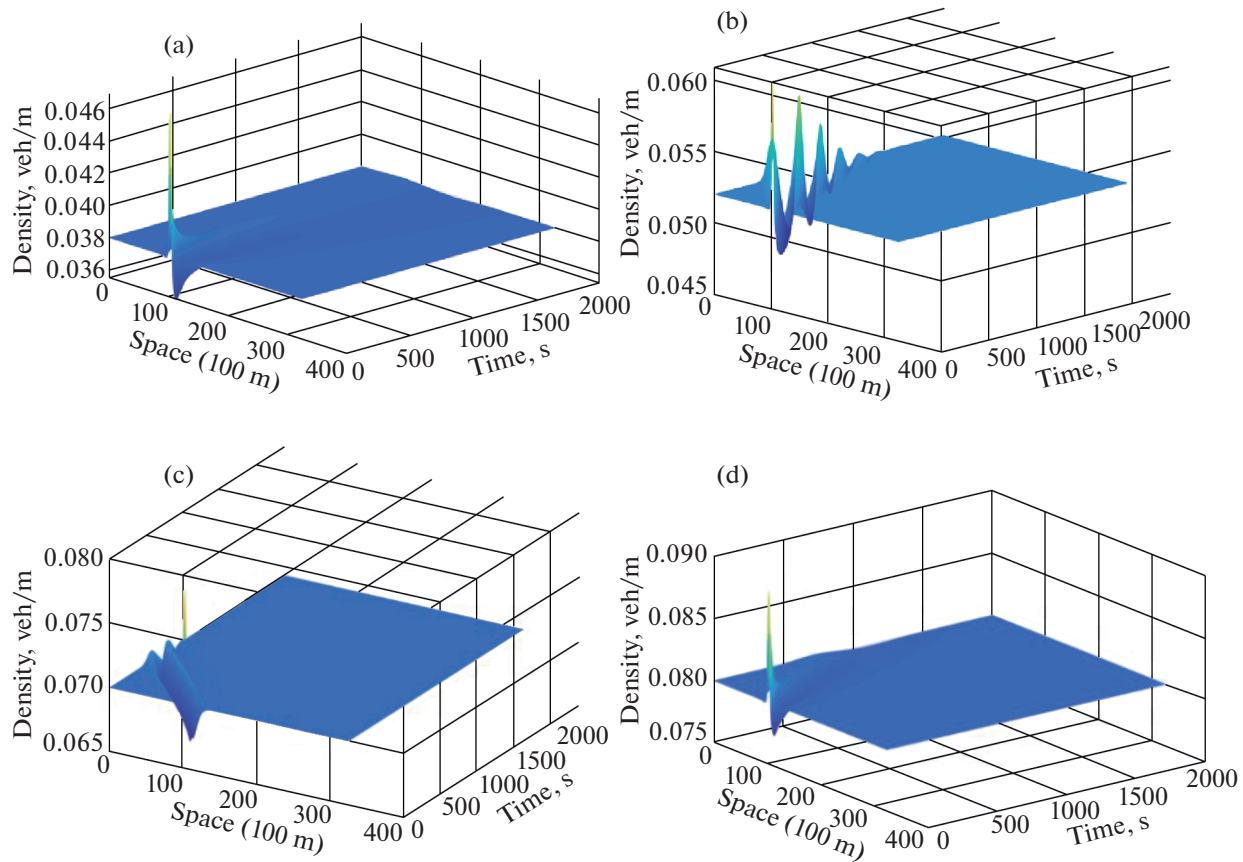


Fig. 2. Spatial and temporal evolution of density waves at various initial densities ρ_0 : (a) 0.038, (b) 0.052, (c) 0.070, and (d) 0.080 veh/m.

To facilitate the simulation, the spatial spacing is taken as equidistant 100 m and the time interval is taken to be equal to 1 s. The other parameters in the model are taken as follows:

$$T = 10 \text{ s}, \quad V_f = 30 \text{ m/s}, \quad \rho_m = 0.2 \text{ veh/m}, \quad \tau = 4 \text{ s}, \quad \text{and} \quad \lambda = 0.4. \quad (4.3)$$

When the parameters are taken as above, the critical densities of the model are equal to 0.045 and 0.070 veh/m, i.e., the traffic flow is linearly unstable when the initial density is in the range of $0.045 < \rho_0 < 0.070$ veh/m.

In Fig. 2 we have reproduced the numerical results at various initial densities. The density fluctuations occur at $\rho_0 = 0.038$ veh/m (Fig. 2a) but they are relatively stable. As the initial density increases, the amplitude of the traffic wave also gradually increases. When $\rho_0 = 0.052$ veh/m (Fig. 2b), a stop-and-go phenomenon takes place. Moreover, when the density reaches $\rho_0 = 0.070$ veh/m (Fig. 2c), the traffic density is similar to the solution described by the Korteweg–de Vries–Burgers equation. Finally, Fig. 2d shows that the steady state will be reached again when the density is greater than $\rho_0 = 0.080$ veh/m. From Figs. 2a–2c it follows that the density wave fluctuates substantially with increase in the traffic density. After reaching 0.080 veh/m, the traffic density reaches the upper boundary. If the density is slightly greater than 0.080 veh/m, the density wave will not amplify and the density wave will eventually disappear. This indicates that the road is more congested under the higher traffic volumes and a small increase in initial density cannot produce density fluctuations in the overall traffic flow. According to the numerical simulation results, the traffic flow is unstable in the region of $0.038 < \rho_0 < 0.080$ veh/m.

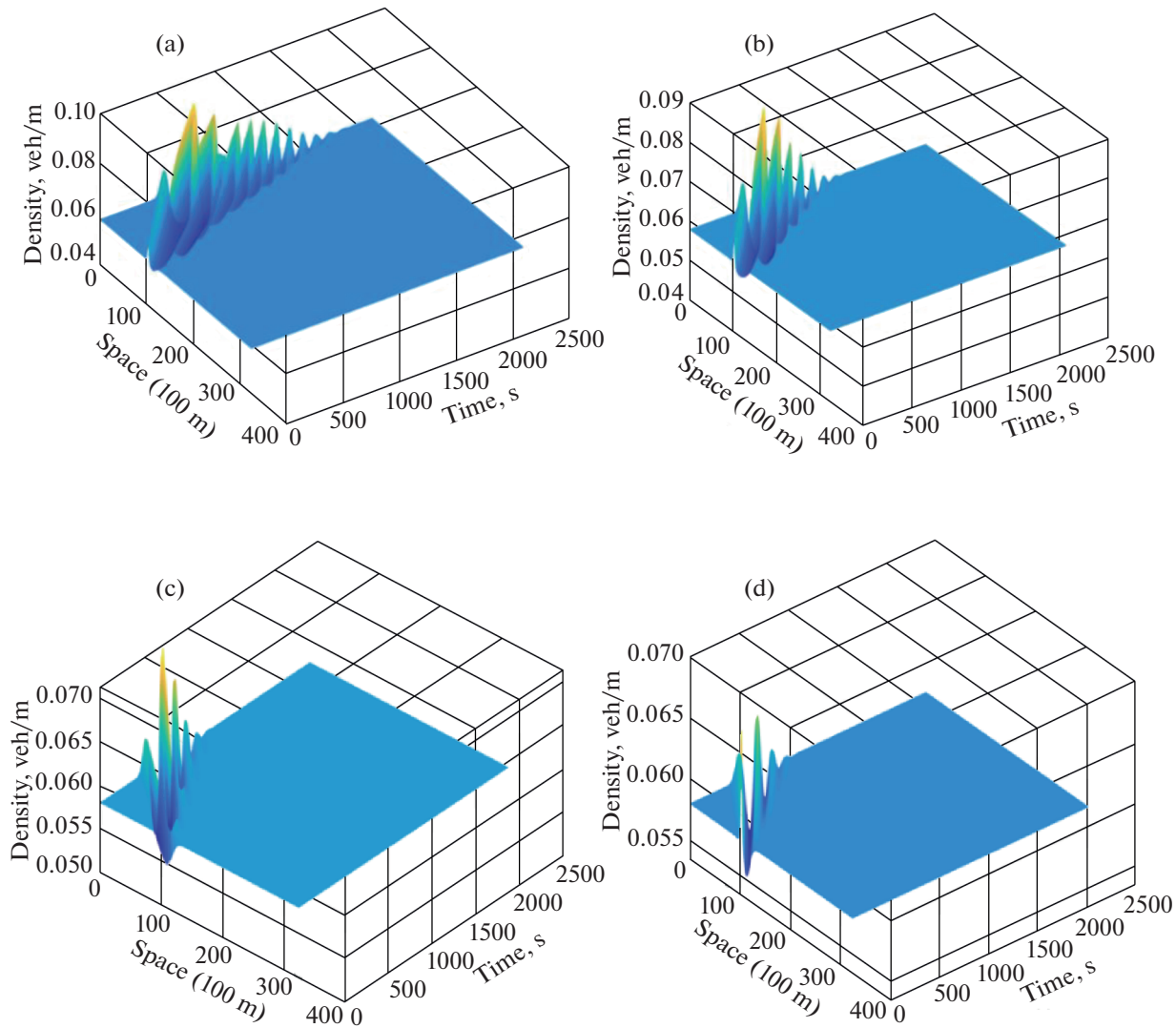


Fig. 3. Evolution of a small perturbation with consideration of various anticipation time τ . (a) $\tau = 0$, (b) 2, (c) 4.3, and (d) 6 s, when $\lambda = 0.3$ at $\rho_0 = 0.065$ veh/m.

4.2. Impact of Various Expected Times on Traffic Flow

To investigate the effect of anticipation time on traffic flow, the following will illustrate the effect of anticipation time on the stability of traffic flow by comparing and analyzing various anticipation times while keeping the values of other parameters constant.

Figure 3 shows the evolution of small perturbations when considering various expected times τ to find the effect on the stability of the system when the expected time is at a fixed value of λ . In the real-world driving environment, the drivers regulate their travel speed by observing the traffic conditions. From the density-time diagram, the density wave is gradually dissipating as the anticipation time τ increases, which indicates that the anticipation effect plays a positive role in the traffic flow stability. The time available to observe traffic conditions becomes longer, and the drivers have plenty of time to adjust their speed.

As shown in Figs. 3a and 3b, the density fluctuation region indicates that the vehicle is in a local blockage state, and the density stabilization region indicates that the vehicle is running freely. In the case of short anticipation time, the drivers are unable to effectively observe the traffic conditions, resulting in frequent stop-and-go motion of vehicles to produce fluctuations, resulting in a local congestion in the lane, indicating that the smaller the anticipation time, the more obvious its effect on the traffic “bottleneck.” In Figs. 3c and 3d, the anticipation time is assumed to be relatively long, and the driver can adjust the speed comfortably. As the anticipation time increases, the range of density fluctuation becomes weaker

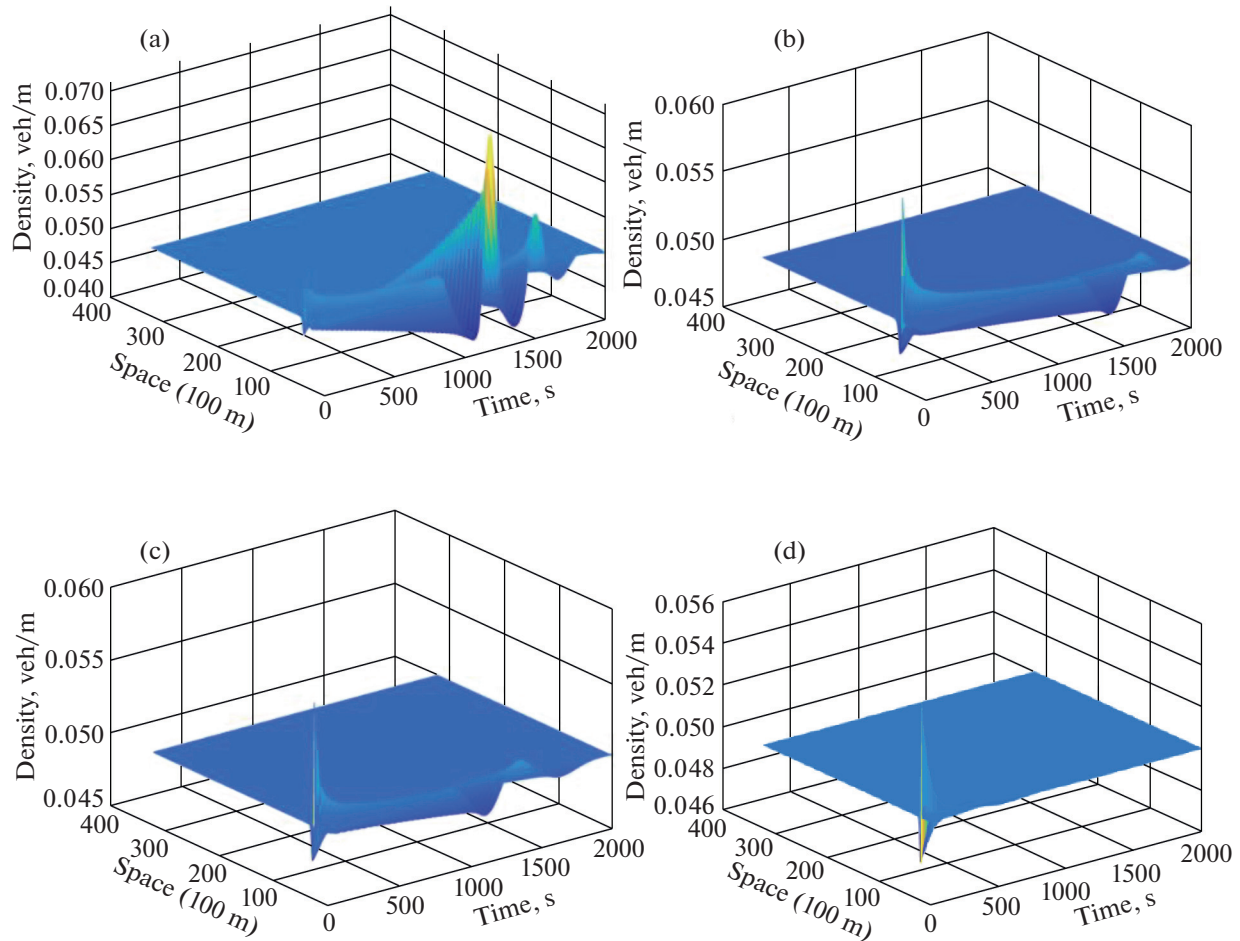


Fig. 4. Evolution of a small perturbation with consideration of various λ : (a) $\lambda = 0.2$, (b) 0.6 , (c) 1.2 , and (d) 2 , when $\tau = 4$ s at $\rho_0 = 0.07$ veh/m.

and the traffic flow tends to be stable, which indicates that the anticipation effect plays a positive role in the traffic flow stability. Therefore, it can be concluded that the expected effect can effectively reduce traffic congestion.

4.3. Influence of Various Jerk Parameters on Traffic Flow

Figure 4 shows the evolution of the small perturbations, and the subsection considers various jerk parameters λ to find the influence of the jerk factors on the system stability. In this part, τ is a fixed value and is taken as $\tau = 4$ s. Figure 4 shows that the density wave becomes very smooth, and the fluctuations are smaller as the jerk parameter λ increases sequentially. So, the jerk plays a positive role in the stability of traffic flow. We can argue that, as compared to the Bando model, considering the jerk effect is effective in mitigating the drastic density fluctuations to a certain extent. The conclusion is shown that traffic jams can be suppressed considering the influence of λ .

4.4. Bifurcation Analysis

When various parameter values are chosen, system (3.24) has different equilibrium points, and the Hopf bifurcation and the saddle-node bifurcation will also differ depending on the equilibrium point. In this section, taking the equilibrium solution of the new model as an example, we can use the software package MATCONT to obtain various system bifurcations by taking different parameters as the continuous variable parameters of the system. The MATCONT is based on the visualization function of MATLAB, which computationally depicts the equilibrium point curves, the limit loops, the doubly peri-

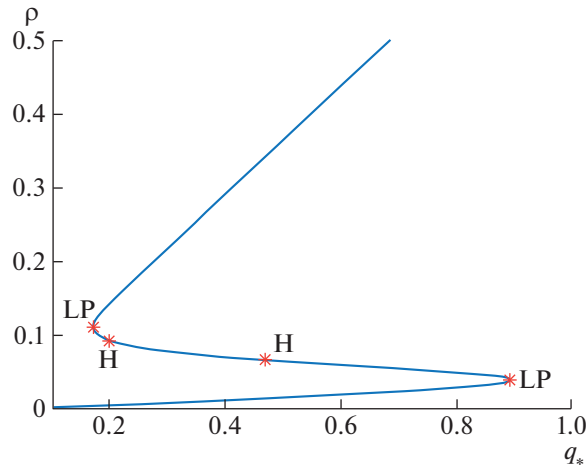


Fig. 5. Bifurcation diagram of ρ – q_* under appropriate parameter intervals.

odic bifurcations, the periodic orbits, the homogeneous orbits and detects various bifurcation points of the system for a system of ordinary differential equations with parameters, such as the Hopf bifurcation, the limit point bifurcation, the limit point bifurcation of cycles, the bifurcation point, the period doubling bifurcation, the cups bifurcation, the Bogdanov–Takens bifurcation, the generalized Hopf bifurcation, etc.

Here, an equilibrium point $(\rho_1, 0) = (0.0065, 0)$ from Subsection 3.2 is used as an example, and the parameter q_* is taken as a variable parameter with an initial value equal to 0.2. We can obtain four special points including two Hopf bifurcations and two limit point bifurcations. This is shown in Fig. 5.

Firstly, the Hopf bifurcation point is selected as the starting point of the bifurcation calculation. When q_* is equal to 0.469940, and the state variable of Hopf bifurcation is (0.067754). It indicates that the vehicle density is equal to $\rho_0 = 0.067754$ veh/m, two characteristic values are equal to $-1.3452e-05 + 0.40864i$ and $-1.3452e-05 - 0.40864i$, respectively. Here, the real part of this pair of conjugate eigenvalues is equal to zero, which is an important condition to determine it as a Hopf bifurcation. Similarly, when q_* is equal to 0.197550, the state variable of Hopf bifurcation obtained is (0.094455), indicating that the vehicle density is $\rho_0 = 0.094455$ veh/m, two characteristic values are equal to $-7.7074e-05 + 0.50039i$ and $-7.7074e-05 - 0.50039i$, respectively.

Then the limit point is taken as the starting point of the bifurcation calculation. When the value of q_* is taken as 0.891695, the limit point state variable is (0.040665), indicating that the vehicle density $\rho_0 = 0.040665$ veh/m at this time, and two eigenvalues are equal to $6.1428e-05$ and -0.098992 , respectively. Here, the latter eigenvalue is equal to zero, which is the marker to determine it as a limit point bifurcation. Another eigenvalue with a negative real part indicates a stable limit point (the saddle junction bifurcation point). Similarly, when the value of q_* is taken to be equal to 0.172588, the limit point state variable is (0.112377), indicating that the density of the vehicle $\rho_0 = 0.112377$ veh/m at this time, and two eigenvalues are equal to $2.1231e-05$ and -0.018227 , respectively. Another eigenvalue with a negative real part indicates a stable limit point (the saddle junction bifurcation point). Substituting the value of ρ_0 in the equation for $-\rho_0^2 V' e(\rho_0)$, we get $-\rho_0^2 V' e(\rho_0) = 0.172588$. The equation $q_{*0} = -\rho_0^2 V' e(\rho_0)$ satisfies the derivation of the saddle-node bifurcation condition of the model, which illustrates the consistency of the theoretical analysis with the numerical results.

Next, the stability of the traffic system is analyzed when the parameters are taken as some of the bifurcation thresholds calculated above. The effect of the Hopf bifurcation on the traffic flow is illustrated by observing the change in the stability of the phase plane diagram of the system as the parameter q_* passes through the values 0.469940 and 0.197550.

We will first examine the change in bifurcation at 0.469940. Here, the parameter $q_* = 0.45$ for parameters less than 0.469940 and $q_* = 0.47$ for parameters greater than 0.469940 are taken.

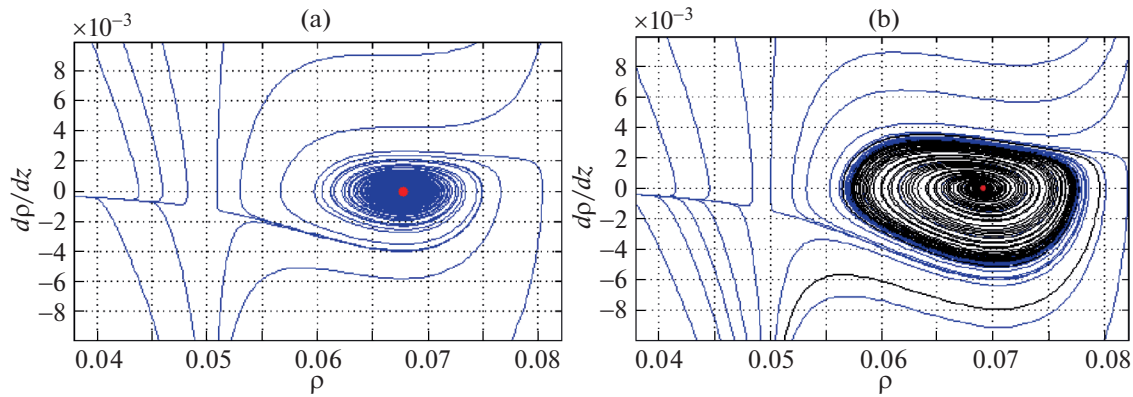


Fig. 6. Phase plane diagram when the parameter q_* passes through the Hopf bifurcation: (a) $q_* = 0.47$ and (b) 0.45.

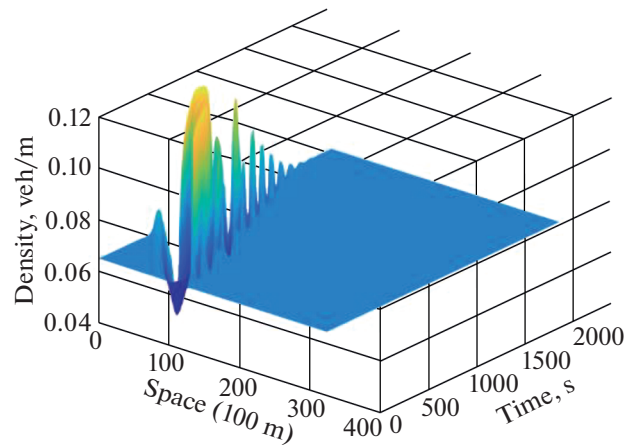


Fig. 7. Space-time plot of the density with the Hopf bifurcation as the initial value.

Figure 6a shows that there is an equilibrium point $(0.067751, 0)$ when the parameter $q_* > 0.469940$. The curve on the left tends to the point $(0.067751, 0)$ and is attracted to it, forming a spiral source. Thus, the system is stable close to $(0.067751, 0)$ and unstable far from $(0.067751, 0)$. Figure 6b shows that a spiral track from $(0.056, 0)$ converges to the focal point $(0.068842, 0)$ as $z \rightarrow +\infty$ and eventually evolves into an equal amplitude oscillation as $z \rightarrow -\infty$ when the parameter $q_* > 0.469940$. However, the other spiral orbital curve is very close to the outside of the above equal amplitude oscillation region as $z \rightarrow -\infty$ and tends to infinity as $z \rightarrow +\infty$. Therefore, there is a periodic solution between the two tracks. Thus, no new equilibrium point emerges at the Hopf bifurcation point, but a periodic solution is generated. These theoretical analyses are also consistent with the numerical results obtained above.

When $q_* = 0.469940$, a limit point bifurcation of cycles appears with the first Lyapunov exponent of $7.750918e + 02$. This exponent is greater than zero, so this Hopf bifurcation is in the sub-critical state and the limit circle is unstable. We can also see the effect of the Hopf bifurcation in the spatial and temporal evolution of the density of traffic flow, as shown in Fig. 7.

The complex phenomenon in congested traffic flow can be easily explained by the evolution of the density time and space diagram over time. The effect of the Hopf bifurcation on traffic flow can be clearly reflected by choosing the state variable ($\rho_0 = 0.067754$ veh/m) of the Hopf bifurcation point as the initial density of the density time and space diagram. According to the property of the Hopf bifurcation, the system generates a periodic solution from the equilibrium point when the parameter passes through the bifurcation point. Since the initial density values at this point are in the unstable range of the model, small perturbations on the initial uniform density are amplified, as shown in Fig. 7, and subsequently evolve into dense oscillations, which are consistent with the characteristics of the solution of the limit loop.

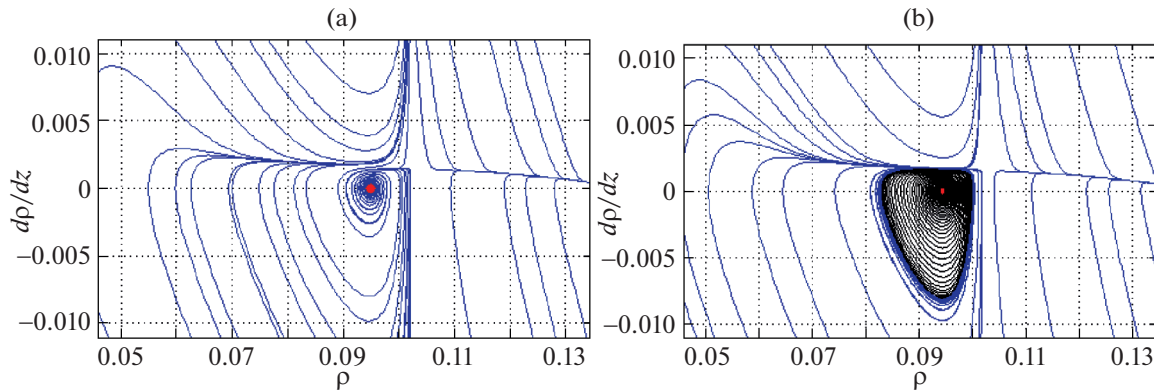


Fig. 8. Phase plane diagram when the parameter q_* passes through the Hopf bifurcation: (a) $q_* = 0.196$ and (b) 0.198 .

This shows that in the case of initially uniform traffic flow, the small disturbance changes to go-stop waves when the parameter is taken as the Hopf bifurcation point state variable and shows that the obtained conclusion is consistent with the actual phenomenon as well as the numerical calculation results, which also verifies the correctness of the theoretical analysis.

Then we analyze the change in bifurcation after 0.197550; here, we take the parameter $q_* = 0.196$ for less than 0.197550 and $q_* = 0.198$ for more than 0.197550.

Figure 8a shows that there is an equilibrium point (0.094915, 0) when the parameter $q_* < 0.197550$. The curve on the right side tends to the point (0.094915, 0) and is attracted by it, forming a spiral source. Thus, the system is stable near the point (0.094915, 0) and unstable far from the point (0.094915, 0). Figure 8b shows that a spiral track from the point (0.082, 0) converges to the focus (0.094325, 0) as $z \rightarrow +\infty$ and eventually evolves to equal amplitude oscillation as $z \rightarrow -\infty$ when the parameter $q_* > 0.197550$. However, the other spiral orbital curve is close to the outside of the above equal amplitude oscillation region as $z \rightarrow -\infty$ and tends to infinity as $z \rightarrow +\infty$. Therefore, there is a periodic solution between the two tracks. Thus, no new equilibrium point emerges at the Hopf bifurcation point, and a periodic solution is generated.

When $q_* = 0.197550$, a limit point bifurcation of cycles appears with the first Lyapunov exponent of $2.535825e + 02$. This exponent is greater than zero, so this Hopf bifurcation is in the sub-critical state, and the limit ring is unstable. We can also see the effect of the Hopf bifurcation in the spatial and temporal evolution of the density of traffic flow.

To study the stability mutation of the system after the saddle-node bifurcation, two saddle-node bifurcations of the model are analyzed separately.

Initially, we will study the bifurcation point $q_* = 0.172588$. When $q_* > 0.172588$, let $q_* = 0.175$, at this point the system has a nodal sink (0.10592, 0) and a saddle point (0.11997, 0), as shown in Fig. 9a. At this point, the trajectory inside the red line is close to the nodal sink, and the trajectory near the saddle point is far from the nodal sink. Thus, the system on the left side of the red line is stable, while the system on the right side of the red line is unstable.

As the value of q_* decreases, the nodal sink and the saddle point gradually move toward the middle. When q_* takes the value of 0.172588, a strange phenomenon occurs, as can be seen in Fig. 9b, namely, the two equilibria seem to merge into a new higher-order equilibrium at the point (0.11238, 0), so the saddle-node bifurcation occurs. Currently, the linear system has a zero eigenvalue. The trajectories within the red line converge at this point, so the traffic system is stable at this location. When q_* decreases to 0.16, the equilibrium point disappears, as shown in Fig. 9c, and all solutions move to the right. The results show that the traffic system becomes unstable.

Then the effect of the limit-loop bifurcation on traffic flow is investigated when $q_* = 0.891695$. When $q_* < 0.891695$, the system has two equilibrium points at this point, a saddle point (0.033662, 0) and a focal point (0.047636, 0). As shown in Fig. 10a, the curve on the right side of the red line tends to the

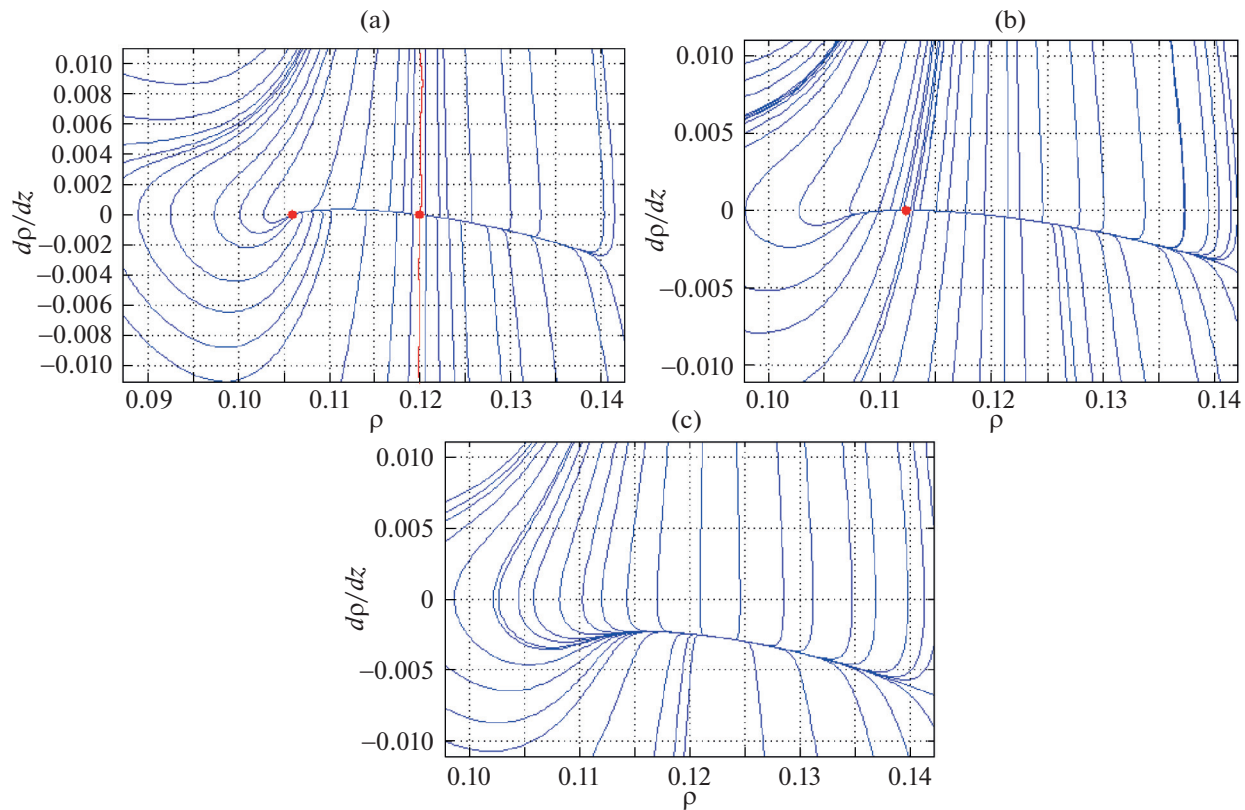


Fig. 9. When parameter q passes through the limit point bifurcation point, the phase plane diagrams of $q_* > 0.172588$, $q_* = 0.172588$, and $q_* < 0.172588$: (a) $q_* = 0.175$, (b) 0.172588 , and (c) 0.16 .

point $(0.047636, 0)$. The traffic state on the right side of the red line is stable. On the contrary, the traffic state on the left side of the red line is unstable.

With increase in q_* , the distance between two equilibrium points keeps shrinking, and when q_* takes the value of 0.891695 , the two points synthesize a new equilibrium point at $(0.040665, 0)$, so the saddle-node bifurcation appears as shown in Fig. 10b. When the value of q_* continues to increase, the equilibrium point disappears and all solutions move to the right, as in Fig. 10c, at which point the whole system becomes unstable.

4.5. Actual Measurement

In this subsection, we will further verify the stability of the static solutions of two traffic flows through the measured data.

In this paper, the measurement method is as follows: a fixed camera above a certain road section is used to capture the traffic flow for a long time, and video software is used to capture the captured video into a single frame image arranged by frame. The traffic video is divided into consecutive single frame images, each image is separated by one second. The traffic data such as the vehicle position, the headway and the speed are extracted from each image. We used the method employed in [59] to extract the traffic data.

First, select any frame picture, for each row of pixels in the picture, each row of pixels must be mapped to the actual distance it represents according to the actual situation. Since the camera has a tilt angle, the angle between each adjacent scan line is equal to α , the corresponding unequal distance in the actual section, after the camera imaging, respectively corresponding to each row of pixels in the image, that is, there is an equal image distance. This shoot is located at the western overpass of the Second Ring South Road in Xi'an. This section traffic video taken by visible link <https://pan.baidu.com/s/1zphCxAt04PTuK5q0vTmiow?pwd=hg66>. Figure 11 is used as an example to illustrate the above extraction method. The calculation principle is shown in Fig. 12.

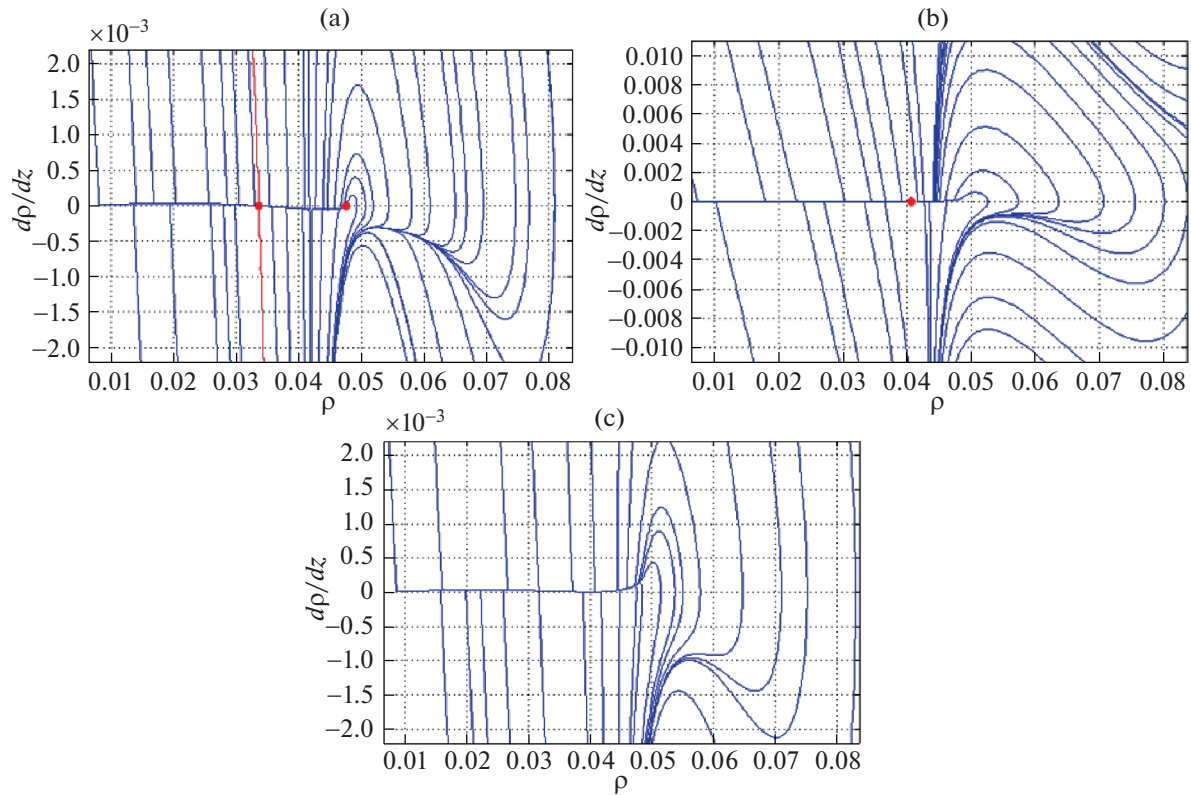


Fig. 10. When parameter q passes through the limit point bifurcation point, the phase plane diagrams of $q^* > 0.891695$, $q^* = 0.891695$, and $q^* < 0.891695$. (a) $q^* = 0.85$, (b) 0.891695 , and (c) 0.9 .



Fig. 11. Video screenshot of the overpass on the west side of Second Ring South Road in Xi'an City.

In Fig. 12, H is the height of the camera above the ground. In our case, $H = 5.5$ m. Point A is located vertically below the camera. Our measurement cross-section starts at point B corresponding to the pixel (294, 480) at the bottom of the right lane line in Fig. 11 and ends at point C corresponding to the pixel (300, 226) at the top of the third right lane marking line in the figure. The distance between points A and

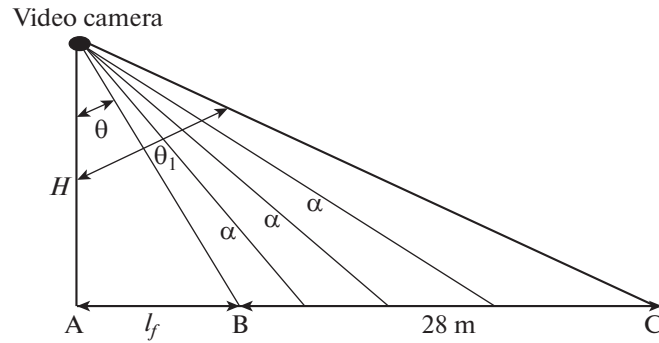


Fig. 12. Actual corresponding camera installation position and imaging schematic diagram.

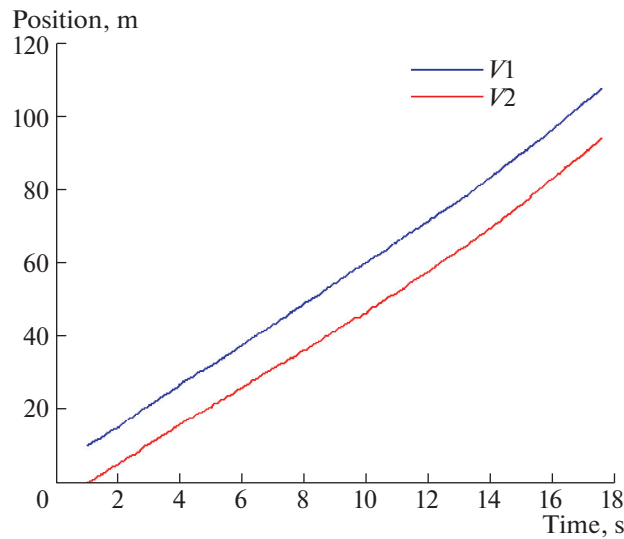


Fig. 13. Vehicle displacement trajectory.

B is equal to 13.5 m. We set it to l_f and the distance between points B and C is equal to 28 m, which corresponds to 254 pixels. So, we have:

$$\theta = \arctan \frac{l_f}{H} = 67.86806039, \tag{4.4}$$

$$\theta_1 = \arctan \left(\frac{28 + 13.5}{5.5} \right) = 82.4923983621193. \tag{4.5}$$

Each row of pixels corresponds to a viewing angle of

$$\alpha = \frac{\theta_1 - \theta}{254} = 0.0575761337398544. \tag{4.6}$$

Setting the pixel value of each row as C, the actual distance corresponding to each row on the image is equal to $H \tan(\theta + C\alpha)$. Meanwhile, the traffic data such as the position, the headway and the speed can be extracted from each frame image.

We selected a set of high-density, low-speed steady-state traffic for validation, and studied ten consecutive sets of vehicles, obtaining 265 sets of data. It is worth pointing out that these consecutive vehicles with an average speed of 5.73 m/s were collected from the same lane for consecutive periods of time, so they are suitable for assessing non-congested traffic conditions.

Figure 13 shows change in the position of the vehicle under test, with the front vehicle and the rear vehicle represented by V1 with blue line and V2 with red line, respectively. The vehicle displacement is proportional to time, so the velocity is constant, at which point it does not change with time. As can be

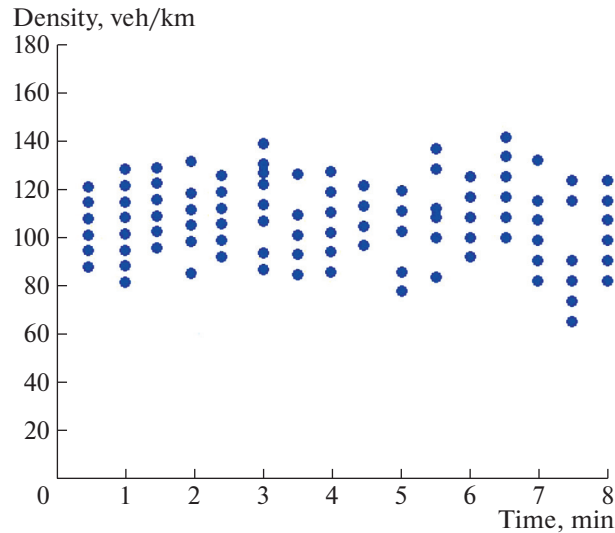


Fig. 14. Density-time scatter plot.

seen from Fig. 14, with increase in time, the traffic density floats between 70 and 142 veh/km, and the traffic density does not vary with time. From the above two figures, it can be seen that the density of vehicles is relatively high and the speed is relatively slow. Currently, the density and speed of traffic flow do not change with time. This state conforms to the stable state of high-density and low-speed traffic flow.

SUMMARY

In this paper, the jerk term representing sharp changes in the acceleration and deceleration speeds in real traffic is added to the conventional optimal velocity model, while the driver's anticipation effect is also considered. A new macroscopic continuous traffic flow model is developed by applying the relationship between microscopic and macroscopic variables based on the improved microscopic car-following model. Then, the linear and nonlinear stability of the model are analyzed, and the neutral stability condition and the Korteweg–de Vries–Burgers equation which can be used to describe the evolution of traffic flow density waves are obtained. Then the effect of driver's anticipation and traffic jerk on the stability of traffic flow in the new model is verified by simulation of the density time and space diagrams. In addition, the type and stability of equilibrium solutions are discussed using the bifurcation analysis method. The theoretical and numerical validations of each other are given. Using the Hopf bifurcation and the saddle-node bifurcation as the starting point, the traffic phenomena such as sudden change in stability on roads are better explained by plotting the density time and space diagram and phase plane diagram of the system. The bifurcation analysis of the model reveals that the stability of the system changes abruptly when the values of the parameters of the system vary and span the values of the Hopf bifurcation point and the saddle-node bifurcation point. Therefore, the study of bifurcation behavior in traffic flow can well explain various nonlinear phenomena in real traffic and provide an effective theoretical basis for guiding and developing the planning and control management of the traffic systems, to achieve the purpose of fundamentally alleviating and preventing traffic congestion.

ACKNOWLEDGMENTS

The authors would like to thank the anonymous referees and the editor for their valuable opinions.

FUNDING

This work is partially supported by the National Natural Science Foundation of China under the Grants nos. 72361031 and 12275223 and the Qizhi Personnel Training Support Project of Lanzhou Institute of Technology (project no. 2018QZ-11) and the University Youth Doctoral Support Project of Gansu Province of China under the Grant no. 2023QB-049.

CONFLICT OF INTEREST

The authors declared that they have no conflicts of interest in this work. We declare that we do not have any commercial or associative interest that represents a conflict of interest in connection with the work submitted.

REFERENCES

1. Karakhi, A., Laarej, A., Khallouk, A., Lakouari, N., and Ez-Zahraouy, H., Car accident in synchronized traffic flow: a stochastic cellular automaton model, *Int. J. Mod. Phys. C*, 2021, vol. 32, no. 1.
2. Vranken, T., Sliwa, B., Wietfeld, C., and Schreckenber, M., Adapting a cellular automata model to describe heterogeneous traffic with human-driven, automated, and communicating automated vehicles, *Phys. A*, 2021, vol. 570, no. 1.
3. Yang, Q.L., Modelling the variation and uncertainty problem of right-turn-on-red queue in a variety of conflicting environments, *Appl. Math. Model.*, 2023, vol. 116, pp. 415–440.
4. Ai, W.H., Zhu, J.N., Zhang, Y.F., Wang, M.M., and Liu, D.W., Bifurcation control analysis based on continuum model with lateral offset compensation, *Phys. A*, 2023, vol. 624, p. 128961.
5. Ai, W.H., Ma, Y.F., and Liu, D.W., Bifurcation analysis based on new macro two-velocity difference model, *Int. J. Geom. Methods M*, 2022, vol. 19, no. 14.
6. Bando, M., Hasebe, K., Nakayama, A., Shibata, A., and Sugiyama, Y., Dynamical model of traffic congestion and numerical simulation, *Phys. Rev. E*, 1995, vol. 51, no. 2, pp. 1035–1042.
7. Helbing, D., Derivation of non-local macroscopic traffic equations and consistent traffic pressures from microscopic car-following models, *C.I.M.E. Summer School*, 2009, vol. 69, no. 4, pp. 539–548.
8. Yu, X., Analysis of the stability and density waves for traffic flow, *Chin. Phys. B*, 2002, vol. 11, no. 11, pp. 1128–1134.
9. Liu, D., Shi, Z.K., and Ai, W.H., An improved car-following model accounting for impact of strong wind, *Math. Probl. Eng.*, 2017, vol. 2017, no. 10, pp. 1–12.
10. Lighthill, M.J. and Whitham, G.B., On kinematic waves. II. A theory of traffic flow on long crowded roads, *Proc. R. Soc. A: Math., Phys. Eng. Sci.*, 1955, vol. 229, no. 1178, pp. 317–345.
11. Richards, P.I., Shock waves on the highways, *Oper. Res.*, 1956, vol. 4, no. 1, pp. 42–51.
12. Payne, H.J., Freflo: a macroscopic simulation model of freeway traffic, *Transportation Research Record*, Transportation Research Board, 1979, issue 772.
13. Whitham, G.B., *Linear and Nonlinear Waves*, New York: Wiley-Intersci., 1974.
14. Aw, A. and Rascle, M., Resurrection of second order models of traffic flow, *Siam J. Appl. Math.*, 2000, vol. 60, no. 3, pp. 916–938.
15. Rascle, M., An improved macroscopic model of traffic flow: derivation and links with the Lighthill–Whitham model, *Math. Comput. Model.*, 2002, vol. 35, no. 5, pp. 581–590.
16. Zhang, H.M., A theory of nonequilibrium traffic flow, *Transp. Res., Part B: Methodol.*, 1998, vol. 32, no. 7, pp. 485–498.
17. Jiang, R., Wu, Q., and Zhu, Z., A new continuum model for traffic flow and numerical tests, *Transp. Res., Part B: Methodol.*, 2002, vol. 36, no. 5, pp. 405–419.
18. Kiselev, A.B., Kokoreva, A.V., Nikitin, V.F., and Smirnov, N.N., Mathematical modelling of traffic flows on controlled roads, *J. Appl. Math. Mech.*, 2004, vol. 68, no. 6, pp. 933–939.
19. Kiselev, A.B., Kokoreva, A.V., Nikitin, V.F., and Smirnov, N.N., Mathematical simulation of two-lane traffic flow controlled by traffic lights, *Moscow Univ. Mech. Bull.*, 2006, vol. 61, no. 4, pp. 1–7.
20. Kiselev, A.B., Nikitin, V.F., Smirnov, N.N., and Yumashev, M.V., Irregular traffic flow on a ring road, *J. Appl. Math. Mech.*, 2000, vol. 64, no. 4, pp. 627–634.
21. Bogdanova, A., Smirnova, M.N., Zhu, Z.J., and Smirnov, N.N., Exploring peculiarities of traffic flows with a viscoelastic model, *Transportmetrica – Transp. Sci.*, 2015, vol. 11, no. 7, pp. 561–578.
22. Smirnova, M.N., Bogdanova, A.I., Zhu, Z., and Smirnov, N.N., Traffic flow sensitivity to visco-elasticity, *Theor. Appl. Mech. Lett.*, 2016, vol. 6, no. 4, pp. 182–185.
23. Zhang, Y.L., Smirnova, M.N., Bogdanova, A.I., Zhu, Z.J., and Smirnov, N.N., Travel time prediction with viscoelastic traffic model, *Appl. Math. Mech.-Engl.*, 2018, vol. 39, no. 12, pp. 1769–1788.
24. Zhang, Y.L., Smirnova, M.N., Bogdanova, A.I., Zhu, Z.J., and Smirnov, N.N., Travel time estimation by urgent-gentle class traffic flow model, *Transp. Res. B – Meth.*, 2018, vol. 113, pp. 121–142.
25. Hu, Z.J., Smirnova, M.N., Zhang, Y.L., Smirnov, N.N., and Zhu, Z.J., Estimation of travel time through a composite ring road by a viscoelastic traffic flow model, *Math. Comput. Simul.*, 2021, vol. 181, pp. 501–521.
26. Huang, Z.M., Smirnova, M.N., Bi, J.R., Smirnov, N.N., and Zhu, Z.J., Analyzing roadway work zone effects on vehicular flow in a freeway ring, *Int. J. Mod. Phys. C*, 2023, vol. 34, no. 4.
27. Hu, Z.J., Smirnova, M.N., Smirnov, N.N., Zhang, Y.L., and Zhu, Z.J., Impacts of down-up hill segment on the threshold of shock formation of ring road vehicular flow, *Adv. Appl. Math. Mech.*, 2023, vol. 15, no. 5, pp. 1315–1334.
28. Li, Z.M., Smirnova, M.N., Zhang, Y.L., Smirnov, N.N., and Zhu, Z.J., Numerical exploration of freeway tunnel effects with a two-lane traffic model, *Simul. T. Soc. Mod. Sim.*, 2023, vol. 99, no. 1, pp. 55–68.
29. Li, Z.M., Smirnova, M.N., Zhang, Y.L., Smirnov, N.N., and Zhu, Z.J., Tunnel speed limit effects on traffic flow explored with a three lane model, *Math. Comput. Simul.*, 2022, vol. 194, pp. 185–197.

30. Schot, S.H., Jerk: the time rate of change of acceleration, *Am. J. Phys.*, 1998, vol. 46, no. 11, pp. 1090–1094.
31. Redhu, P. and Siwach, V., An extended lattice model accounting for traffic jerk, *Phys. A*, 2018, vol. 492, pp. 1473–1480.
32. Liu, Y., Cheng, R.J., Lei, L., and Ge, H.X., The influence of the non-motor vehicles for the car-following model considering traffic jerk, *Phys. A*, 2016, vol. 463, pp. 376–382.
33. Sun, F.X., Wang, J.F., Cheng, R.J., and Ge, H.X., An extended heterogeneous car-following model accounting for anticipation driving behavior and mixed maximum speeds, *Phys. Lett. A*, 2018, vol. 382, no. 7, pp. 489–498.
34. Wan, J., Huang, X., Qin, W.Z., Gu, X.G., and Zhao, M., An Improved lattice hydrodynamic model by considering the effect of backward-looking and anticipation behavior, *Complexity*, 2021, vol. 2021, p. 4642202.
35. Tian, J.F., Yuan, Z.Z., Jia, B., Li, M.H., and Jiang, G.J., The stabilization effect of the density difference in the modified lattice hydrodynamic model of traffic flow, *Phys. A*, 2012, vol. 391, no. 19, pp. 4476–4482.
36. Zhao, M., Sun, D.H., and Tian, C., Density waves in a lattice hydrodynamic traffic flow model with the anticipation effect, *Chin. Phys. B*, 2012, vol. 21, no. 4, pp. 623–628.
37. Yu, L. and Zhou, B.C., The burgers equation for a new continuum model with consideration of driver's forecast effect, *J. Appl. Math.*, 2014, vol. 2014, pp. 1–7.
38. Li, Z.B., *Traveling Wave Solution of Nonlinear Mathematical Physics Equations*, Science Press, 2007.
39. Lai, L.L., Cheng, R.J., Li, Z.P., and Ge, H.X., The KdV–Burgers equation in a modified speed gradient continuum model, *Chin. Phys. B*, 2013, vol. 22, no. 6, pp. 293–297.
40. Liu, H.Q., Zheng, P.J., Zhu, K.Q., and Ge, H.X., KdV–Burgers equation in the modified continuum model considering anticipation effect, *Phys. A*, 2015, vol. 438, pp. 26–31.
41. Ai, W.H., Zhang, T., and Liu, D.W., Bifurcation analysis of macroscopic traffic flow model based on the influence of road conditions, *Appl. Math.-Czech.*, 2023, vol. 68, no. 4, pp. 499–534.
42. Ai, W.H., *Research on Branch Analysis Method of Traffic Flow Nonlinear Phenomenon*, Northwestern Polytechnical Univ., 2016.
43. Igarashi, Y., Itoh, K., Nakanishi, K., Ogura, K., and Yokokawa, K., Bifurcation phenomena in the optimal velocity model for traffic flow, *Phys. Rev. E*, 2001, vol. 64, no. 4.
44. Li, T., Nonlinear dynamics of traffic jams, *Phys. D*, 2005, vol. 207, no. 1, pp. 41–51.
45. Delgado, J. and Saavedra, P., Global bifurcation diagram for the Kerner-Konhauer traffic flow model, *Int. J. Bifurcation Chaos*, 2015, vol. 25, no. 5.
46. Ai, W.H., Shi, Z.K., and Liu, D.W., Bifurcation analysis of a speed gradient continuum traffic flow model, *Phys. A*, 2015, vol. 437, pp. 418–429.
47. Cheng, L.F., Wei, X.K., and Cao, H.J., Two-parameter bifurcation analysis of limit cycles of a simplified railway wheelset model, *Nonlin. Dyn.*, 2018, vol. 93, no. 4, pp. 2415–2431.
48. Ai, W.H., Zhu, J.N., Duan, W.S., and Liu, D.W., A new heterogeneous traffic flow model based on lateral distance headway, *Int. J. Mod. Phys. B*, 2021, vol. 35, no. 23, pp. 1–19.
49. Ai, W.H., Li, N., Duan, W.S., Tian, R.H., and Liu, D.W., Bifurcation analysis of a modified continuum traffic flow model considering driver's reaction time and distance, *Int. J. Mod. Phys. C*, 2023, vol. 34, no. 3.
50. Liu, G., Lyrintzis, A., and Michalopoulos, P., Improved high-order model for freeway traffic flow, *Transp. Res. Rec.*, 1998, vol. 1644, no. 1, pp. 37–46.
51. Kurtze, D.A. and Hong, D.C., Traffic jams, granular flow, and soliton selection, *Phys. Rev. E*, 1995, vol. 52, no. 1, pp. 218–221.
52. Nagatani, T., The physics of traffic jams, *Rep. Prog. Phys.*, 2002, vol. 65, no. 9, pp. 1331–1386.
53. Helbing, D. and Tilch, B., Generalized force model of traffic dynamics, *Condens. Matter*, 1998, vol. 58, no. 1, pp. 133–138.
54. Berg, P. and Woods, A., On-ramp simulations and solitary waves of a car-following model, *Phys. Rev. E*, 2001, vol. 64, no. 3.
55. Aulbach, B. and Wanner, T., The Hartman–Grobman theorem for Caratheodory-type differential equations in Banach spaces, *Nonlin. Anal.-Theor.*, 2000, vol. 40, no. 1, pp. 91–104.
56. Kerner, B.S. and Konhuser, P., Cluster effect in initially homogeneous traffic flow, *Phys. Rev. E*, 1993, vol. 48, no. 4, pp. 2335–2338.
57. Cao, J.F., Han, C.Z., and Fang, X.W., *Theory and Application of Nonlinear Systems*, Xi'an Jiaotong Univ. Press, 2006.
58. Daganzo, C.F. and Laval, J.A., Moving bottlenecks: A numerical method that converges in flows, *Transp. Res. B-Meth.*, 2005, vol. 39, no. 9, pp. 855–863.
59. Shuming, R., Traffic speed measurement based on video, *Comput. Commun.*, 2007, vol. 25, pp. 90–93.

Publisher's Note. Pleiades Publishing remains neutral with regard to jurisdictional claims in published maps and institutional affiliations.